NOX4 inhibition potentiates immunotherapy by overcoming cancer-associated fibroblast-mediated CD8 T-cell exclusion from tumors

Kirsty Ford[1], Christopher J. Hanley[1], Massimiliano Mellone[1], Cedric Szyndralewiez[2], Freddy Heitz[2], Philippe Wiesel[2], Oliver Wood[1], Maria Machado[1], Maria-Antoinette Lopez[1], Anusha-Preethi Ganesan[3], Chuan Wang[1], Ankur Chakravarthy[4], Tim R. Fenton[5], Emma V. King[1], Pandurangan Vijayanand[3], Christian H. Ottensmeier[1], Aymen Al-Shamkhani[1], Natalia Savelyeva[1], Gareth J. Thomas[1*]

[1]Cancer Sciences Unit, Faculty of Medicine, University of Southampton, Southampton, SO16 6YD, UK. [2]Genkyotex SA, Geneva, 1228, Switzerland. [3]La Jolla Institute for Allergy & Immunology, La Jolla, California, 92037, USA. [4]Department of Medical Biophysics, University of Toronto, Toronto, ON M5G 1L7, Canada. [5]School of Biosciences, University of Kent, Canterbury, CT2 7NJ, UK.

Running title: CAF-targeting by NOX4 inhibition potentiates immunotherapy

Keywords:

cancer-associated fibroblast, immunotherapy, checkpoint-blockade, NOX4, TGF-β, CTLA-4

Financial support. Funded through Cancer Research UK (grant nos. A203904, A20256, A27989) and Medical Research Council UK (grant no. MR/P013414/1 & CASE Studentship for KF [with Genkyotex]).

Conflict of Interest statement.

The authors declare no competing financial or other interests.

*Corresponding author
Gareth J Thomas
Address: Cancer Sciences Unit, Faculty of Medicine, University of Southampton, Tremona Road
Southampton SO16 65YD
e-mail: g.thomas@soton.ac.uk
Tel: +44 7845 361124

Abstract

Determining mechanisms of resistance to αPD-1/PD-L1 immune checkpoint immunotherapy is key to developing new treatment strategies. Cancer-associated fibroblasts (CAF) have many tumor-promoting functions and promote immune evasion through multiple mechanisms, but as yet, there are no CAF-specific inhibitors clinically available. Here we generated CAF-rich murine tumor models (TC1, MC38, 4T1) to investigate how CAF influence the immune microenvironment and affect response to different immunotherapy modalities (anti-cancer vaccination; TC1, [HPV E7 DNA vaccine]; αPD-1, MC38) and found that CAFs broadly suppressed response by specifically excluding $CD8^+$ T-cells from tumors (not $CD4^+$ T-cells or macrophages); $CD8^+$ T-cell exclusion was similarly present in CAF-rich human tumors. RNA sequencing of $CD8^+$ T-cells from CAF-rich murine tumors and immunochemistry analysis of human tumors identified significant upregulation of CTLA-4 in the absence of other exhaustion markers; inhibiting CTLA-4 with a non-depleting antibody overcame the $CD8^+$ T-cell exclusion effect without affecting T-regs. We then examined the potential for CAF targeting, focusing on the ROS-producing enzyme NOX4, which is upregulated by CAF in many human cancers, and comparing this to TGF-β1 inhibition, a key regulator of the CAF phenotype. siRNA knockdown or pharmacological inhibition (GKT137831 [Setanaxib]) of NOX4 'normalized' CAF to a quiescent phenotype and promoted intratumoral $CD8^+$ T-cell infiltration, overcoming the exclusion effect; TGF-β1 inhibition could prevent, but not reverse, CAF differentiation. Finally, NOX4 inhibition restored immunotherapy response in CAF-rich tumors. These findings demonstrate that CAF-mediated immunotherapy resistance can be effectively overcome through NOX4 inhibition, and could improve outcome in a broad range of cancers.

Significance: NOX4 is critical for maintaining the immune-suppressive cancer-associated fibroblast (CAF) phenotype in tumors. Pharmacological inhibition of NOX4 potentiates immunotherapy by overcoming CAF-mediated $CD8^+$ T-cell exclusion.

Introduction

Immune checkpoint inhibitors that target PD-1/PD-L1 and CTLA-4 are used to treat an ever-expanding range of malignancies (1-3). Their success has led to a burgeoning interest in other immunotherapy approaches, such as cancer vaccines and adoptive cell transfer (4). However, most patients (~80%) fail to respond to checkpoint monotherapy, a fact that highlights the need to identify targetable resistance mechanisms to broaden clinical effectiveness of these drugs (5,6).

The success of most immunotherapies relies on $CD8^+$ T-cells effectively infiltrating tumors (7). Significantly, non-responders to immunotherapy have been shown to display an 'immune excluded' tumor phenotype where lymphocytes fail to penetrate the tumor (8-10). Recent tissue analyses from αPD-1-treated tumors have also identified a prominent CAF gene signature in non-responders, marked by upregulation of genes regulating extracellular matrix (ECM) remodeling and TGF-β1 signaling (6,10,11).

While CAF remain a relatively poorly characterized heterogenous cell population, the term CAF most commonly refers to cells with a myofibroblast-like phenotype; similar to myofibroblasts, CAF typically transdifferentiate through TGF-β1 signaling, generating a contractile cell, which expresses αSMA, secretes collagen-rich ECM and promotes multiple hallmarks of malignancy (12-16). CAF-containing tumors often have low levels of lymphocytes, and recent studies suggest an emerging role for CAF in tumor immune evasion (9,17). This raises the possibility that CAF-targeting could produce immunotherapeutic benefit. Treatments designed to target CAF however, have not been successful clinically because the identification of specific CAF targets has proven problematic (18-20). Previously we identified the role of NOX4 in regulating CAF differentiation (21). This ROS-producing enzyme is a downstream target of TGF-β1, and a central, and relatively specific regulator of the CAF phenotype in multiple human cancers (21).

The principal aims of this study were to examine the effect of CAF on different immunotherapies, to investigate how CAF affect immune cell phenotype, function and distribution, and to explore the use of a small molecule NOX4 inhibitor (GKT137831 [Setanaxib]) for CAF-targeting in combination with immunotherapy.

Methods

Murine tumor models. Experiments were conducted according to UK Home Office Regulations (license number P8969333C) and received appropriate institutional approval. C57BL/6J or BALB/c WT mice were originally obtained from Charles River Laboratories and colonies maintained in-house. The following tumor models were used in the study; murine lung cancer cell line, TC1 (obtained from ATCC), derived from C57BL/6 murine lung epithelial cells immortalized with HPV-16 E6 and E7 and transformed with c-Ha-ras (22). Murine colorectal cancer cell line, MC38 (obtained from Charles River Laboratories) derived from a methylcholanthrene-induced C57BL/6 murine colon adenocarcinoma (23). Murine breast cancer cell line 4T1 (obtained from ATCC), derived from a spontaneously arising BALB/c mammary tumor (24). 0.5 x 10^5 TC1 or MC38 cancer cells were injected in phosphate-buffered saline (PBS) subcutaneously (s.c) into the flank of C57BL/6 female mice aged 8-10 weeks. TC1 or MC38 cells were either injected alone, or mixed with 2.5 x 10^5 C57BL/6 lung or colon fibroblasts respectively, which had been pre-treated *ex vivo* prior to injection with 2 ng/ml of TGFβ1 (R&D Systems) for 6 days to induce a myofibroblast CAF-like phenotype. 0.25 x 10^5 4T1 cancer cells in PBS were injected s.c into the upper mammary fat pad of female mice aged 8-10 weeks. Cells were either injected alone, or mixed with 1.25x10^5 BALB/c breast CAF isolated from transgenic BALB-neuT spontaneous breast tumors (25). Tumors were measured every 2-3 days by electronic skin caliper from longest width and length and tumor volume calculated using the formula $4/3\pi Xr^3$ where the radius (r) was calculated from tumor width and length measurement to provide an average diameter value. Mice were placed into groups based on tumor volume so that there was no statistical difference in mean tumor volumes between groups before treatment commenced. Vaccination with DNA vaccine encoding tetanus Fragment C domain 1 (Dom) (26) fused to the immunodominant CD8 epitope of E7 HPV RAHYNIVTF (RAH, $E7_{49-57}$) p.Dom-RAH was administered via intramuscular injection (i.m) when tumors were palpable. P.Dom without the epitope served as a control. One injection containing 50 µg of DNA in PBS was given and any repeat doses were given 3 weeks post

initial immunisation (27). NOX4 inhibitor GKT137831 (Setanaxib, Genkyotex SA, Switzerland) was reconstituted in 1.2% Methyl Cellulose (Sigma) with 0.1% Polysorbate (Sigma) and administered to mice by oral gavage 5X/wk at 40 mg/kg when tumors were palpable. Control mice received vehicle alone. For longer term dosing, 15 initial doses were given as stated, but reduced to 3X/wk for 3 weeks at 50 mg/kg, and finally 2X/wk for 3 weeks at 60 mg/kg to comply with UK home office project license procedure limits for repeated oral gavage. αPD-1 antibodies (Bioxcell; RMP1-14) were given via intraperitoneal (i.p) injection. 300 µg of antibody or IgG2a isotype control (Bioxcell) were given when tumors were palpable every other day, totaling 3 doses. αCSF-1 antibodies (Bioxcell; 5A1) were given via (i.p) injection. Initially 1 mg of antibody or IgG1 isotype control (Bioxcell) was given when tumors were palpable then a further 4 doses were given at 500 µg spaced 4 days apart. αCTLA-4 blocking antibodies (Bioxcell; 9D9) were given via i.p injection. 200 µg of antibody or IgG2b isotype control antibodies (Bioxcell) were given when tumours were palpable every three days, totalling 3 doses. αTGF-b1 antibodies (Bioxcell; 1D11) were given via i.p injection. 200 µg of antibody or IgG1 isotype control antibodies (Bioxcell) were given when tumours were palpable every other day totalling 5 doses.

Cell culture and treatments. TC1 cells (ATCC) were cultured in RPMI 1640 (Sigma) supplemented with 10% FBS and 2 mM L-glutamine (Sigma G7513). MC38 cells (Charles River Laboratories) were cultured in DMEM (Sigma D5671) with 10% FBS, HEPES (Gibco 15630-056), non-essential amino acids (Sigma M7145), Sodium pyruvate (Sigma 58636) and L- glutamine. 4T1 (ATCC) were cultured in DMEM with 10% FBS and L-glutamine. Lung fibroblasts were isolated from C57BL/6 female mice; pieces of tissue were washed 3X in fresh PBS containing 4% penicillin/streptomycin and 0.25 µg/ml amphotericin B (Sigma) and grown in 12-well tissue culture plates (Corning) in 750 µL of DMEM containing 20% FBS, 4% penicillin/streptomycin and amphotericin B. Tissue pieces were cultured for 5 days and medium changed twice weekly. As cells appeared from the tissue, penicillin/streptomycin concentration

was lowered to 2%. At 80% confluence, cells were detached with 0.05% trypsin/EDTA solution (Sigma-Aldrich). Cells from adjacent wells were pooled and expanded into one T75 tissue culture vented flask (Corning) containing DMEM, 10% FBS, L-glutamine 1% penicillin/streptomycin and amphotericin B. BALB/c breast CAF and normal fibroblasts (NOFs) were isolated similarly from BALB-neuT transgenic spontaneous breast tumors or WT breast tissue respectively. Primary C57BL/6 colon fibroblasts (Cell Biologics) were maintained in DMEM containing 10% FBS, 2 mM L-glutamine, 1% penicillin/streptomycin and amphotericin B. All fibroblasts were cultured at 37°C, 5% CO_2 and 3% O_2. 1 x 10^5 fibroblasts were seeded per 6-well for PCR analysis or 5 x 10^3 per 8-well chamber slides for immunofluorescence analysis and left to culture for 48h. Cells were treated with 40 μM GKT137831 for 1 hour followed by 2 ng/ml TGFβ1 treatment. To assess the effect of drugs on myofibroblastic CAF differentiation, fibroblasts were treated with 40 μM GKT137831 or 25 μg/ml of αTGFβ (Bioxcell for 1 hour followed by 2 ng/mL TGFβ1 treatment. To test the effect of drug on the established CAF phenotype, inhibitors were directly applied to CAF. Cells were then cultured for 48h for PCR analysis, 72h for ROS analysis or 6-days for immunofluorescence (unless otherwise stated). For 6-day experiments, cells were re-treated with agents as above after 3 days. All cell lines were routinely pcr-tested for Mycoplasma.

RNA interference. Lentiviral mediated shRNA transduction was used to stably knock-down NOX4 in fibroblasts. To generate lentiviral particles, HEK-293-T-cells were transiently transfected with 3 μg pLKO.1 lentiviral vector (Sigma) containing shNOX4 or sh non-targeting control (Sigma) plus 3 μg of pCMVDR8.91 and 0.75 μg of pMD.2G plasmids (Addgene) using transfection reagent Lipofectamine 2000 (Invitrogen). Fibroblasts were transduced with lentiviral particles plus 0.4 μg/ml polybrene (Sigma) and infected overnight. Virally transduced fibroblasts were selected by adding 0.75 μg/ml puromycin (Sigma).

Flow cytometry. Antibodies and clones used were anti-CD45.5-percp-Cy5.5 (104), anti-CD3-eFluor-450 (17A2), anti-CD4-eFluor-450 (GK1.5), anti-CD8a-APC-Cy7 (53-6.7), anti-PD-1-PE (RMP1-30), anti-CTLA-4-PE (UC10-4B9), anti-CD11b-PE (M1/70), anti-F480-APC-Cy7 (BM8), anti-TNFα-PE-Cy7 (MP6-XT22), anti-granzyme B-APC (GB11) viability dye eFluor-450 and appropriate isotype controls (all from e-Bioscience/Thermofisher) as well as anti-CD3-FITC (17A2), anti-IRF4-AF488 (IRF4.3E4), anti-CD137-APC (17B5), anti-IFNγ-FITC (XMG1.2) and appropriate isotype controls (all Biolegend), anti-Ki67-FITC (BD Pharmingen) and DAPi for staining dead cells (Invitrogen). E7 tetramer was made in-house using the RAHYNIVTF 9-mer peptide and PE labelled. For analysis of total tumor infiltrating immune cells, tumors were cut into small pieces and incubated at 37°C for 20 minutes in a shaking incubator in complete RPMI 1640 medium containing 0.15 Wünsch Unit/ml Liberase TL (Sigma Aldrich) and 50 µg/ml DNAse 1 (Sigma Aldrich). Tumors were mashed through a 100 µm strainer (Greiner Bione) and pelleted by centrifugation at 500g for 5 minutes to achieve a single cell suspension. Red blood cells were lysed for 5 minutes at RT with RBC lysis solution (eBioscience) before staining. For all flow cytometry, single cell suspensions were incubated with 10 µg/ml anti-Fc receptor mAb (2.4G2, BD) for 10 minutes at 4 °C prior to surface staining. Antibodies were added at a concentration of 10 µg/ml and incubated for 30 minutes at 4 °C in the dark. Samples were washed with FACS buffer containing PBS with 0.1% BSA, centrifuged for 5 minutes at 200g and run on a flow cytometer (BD FACS Canto). For intracellular/intranuclear staining, cells were fixed and permeabilized post surface staining using FOXP3 staining buffer set (e-Bioscience) and antibodies applied for 30 minutes at 4 °C in the dark. Cells were washed for 5 minutes at 200g in permeabilization buffer and analyzed. For detection of intracellular cytokines, tumor single cell suspension was re-stimulated for 5 hours with 1 µg/mL of relevant peptide (E7 predefined epitope) in the presence of Golgi plug and Golgi stop (BD Pharmingen). After surface staining, cells were fixed, permeabilized with BD cytofix/perm (BD Pharmingen) and intracellular cytokine staining performed in permeabilization buffer. Single stain control tubes were used to set appropriate voltages and isotype controls were used to aid the gating of

positive populations. Stained cells or fluorescent beads (BD Pharmingen) were used for compensation set up. FlowJo (Tree star) software was used for analysis.

RNA extraction and RT-qPCR. RNA extraction was performed using an RNEasy mini kit (Qiagen) following the standard protocol. mRNA was retro-transcribed using RevertAid First Strand cDNA Synthesis Kit (Thermo Scientific) following the manufacturer's instructions. RT-qPCR was performed with SYBR green reagent (Life Technologies). Analysis of relative gene expression was performed in ΔΔCT by comparing the gene of interest CT value to housekeeping gene HPRT CT value. Data was normalized to TGFβ1-treated positive control. Primer sequences and concentrations used were, ACTA2, 0.1 µM, F:CCTCATGCCATCATGCGTCT / R:AATCTCACGCTCGGCAGTAG, COL1A1, 0.4 µM, F:GTGTTCCCTACTCAGCCGTC / R:ACTCGAACGGGAATCCATCG, COL3A1, 0.2 µM, F:TCCTGGTGGTCCTGGTACTG / R:AGGAGAACCACTGTTGCCTG, FN1, 0.1 µM, F:GAAGACAGATGAGCTTCCCCA / R:GGTTGGTGATGAAGGGGGTC, NOX4, 0.4 µM, F:TGCCCCAGTGTATCAGCATT / R:CCGGAATCGTTCTGTCCAGT, HPRT1, 0.1 µM, F:GTTGGGCTTACCTCACTGCT / R:TCATCGCTAATCACGACGCT.

Bulk RNA sequencing and analysis. Total RNA was purified using a miRNAeasy micro kit (Qiagen, USA) and quantified as described (28). Purified total RNA was amplified following the smart-seq2 protocol. cDNA was purified using AMPure XP beads (0.9:1 ratio, Beckman Coulter). From this step, 1 ng of cDNA was used to prepare a standard Nextera XT sequencing library (Nextera XT DNA sample preparation kit and index kit, Illumina) (29). Samples were sequenced using HiSeq2500 (Illumina) to obtain 50-bp single-end reads. Quality control steps were included to determine total RNA quality and quantity, optimal number of PCR pre-amplification cycles, and cDNA fragment size. Samples that failed quality control were eliminated from further analysis. Bulk RNA-seq data were mapped against the mm10 reference using TopHat (30) (v1.4.1) (--library-type fr-unstranded --no-coverage-search) with FastQC

(v0.11.2), Bowtie (31) (v1.1.2), Samtools (32) (0.1.18) and we employed htseq-count -m union -s no -t exon -i gene_id (part of the HTSeq framework, version 0.7.1) (33). Values throughout are displayed as log_2 TPM (transcripts per million) counts; a value of 1 was added prior to log transformation. To identify genes differentially expressed between 2 groups, we performed negative binomial tests for unpaired comparisons by employing the Bioconductor package DESeq2 (v1.14.1) disabling the default options for independent filtering and Cooks cutoff (34). We considered genes differentially expressed between any comparison when the DESeq2 analysis resulted in a Benjamini-Hochberg–adjusted *P* value <0.05. The Qlucore Omics Explorer 3.2 software package was used for visualization and representation (heat map) of RNA-Seq data (28). GSEA were performed as previously described (35,36). Genes used in the GSEA analysis are shown (Supplementary Table S2) (37).

Weighted Gene Correlation Network Analysis (WGCNA) was performed on publicly available HNSCC RNA-Seq data (38) (data are available at: ArrayExpress accession E-MTAB-4546) using the wgcna R package (39). Raw counts were transformed as described above (log2(TPM + 1)) and batch effects between datasets removed using the limma package in R (40). Genes used as input for WGCNA were determined by performing principal components analysis (PCA) and selecting components that accounted for ~95% of the variance within the data. Genes were ranked by highest absolute PCA score to one of these components and the top 8000 were selected for use in WGCNA. Modules were identified from unsupervised hierarchical clustering of genes using 1-Topological overlap, within a scale-free adjacency matrix, as a distance measure. Each module was then summarized by the first principal component gene (module eigengene – ME; representing a suitably defined average of the gene module). GO Biological processes and KEGG Pathway enrichment analyses were carried using GSEA where all genes were ranked by their correlation to the module eigengene using the fgsea package in R (25).

Histological analysis. For IHC of αSMA (Sigma Aldrich; 1A4), tissues were fixed in 4% paraformaldehyde and embedded in paraffin. 4 µm sections were de-paraffinized, rehydrated and antigen retrieved for 20 minutes at 97°C using a predefined program on the Dako PT links. Antigen retrieval was performed using Envision FLEX High pH. Endogenous peroxidase activity was blocked using 3% hydrogen peroxide. Mouse Ig blocking reagent (M.O.M kit vector labs) was applied for 1 hour. Primary antibody incubation (1:100) in M.O.M diluent (vector labs) was for 20 minutes. For secondary amplification, M.O.M. Biotinylated anti-Mouse IgG reagent was applied for 10 minutes followed by Vectorstain elite ABC reagent (vector labs). Chromogenic visualization was completed with 2x5 minute washes in DAB and counterstaining with Haematoxylin. For IHC of CD8 (in house; YTS169), CD4 (BD; RM4-5), PD-L1 (Thermo Fisher; MIH5) and F480 (AbD Serotec; Cl:A3-1) tissues were frozen in OCT. 8 µm sections were fixed in 100% acetone for 10 minutes. Endogenous peroxidase activity was blocked using neat peroxidase suppressor (Peirce) for 15 minutes. Sections were blocked for 30 minutes with 2.5% goat serum. Primary antibodies were applied for 2 hours -CD8 (1:800), CD4 (1:100), F480 (1:100). Appropriate species HRP polymer (ImmunoPress, Vector Laboratories) was applied to sections for 30 minutes. Vector NovaRED chromagen substrate (Vector Laboratories) was applied for 2-10 minutes then counterstained with haematoxylin (Vector Laboratories) for 30 seconds. Images were captured using an Olympus CKX41 microscope with Cell B imaging software. % area of staining was calculated using Fiji software (java) by running the 'color deconvolution' tool analyzing H DAB. The image was appropriately thresholded based on the 'color 2' image. The same thresholding was applied to all images from the same experiment. Regions of interest (margin & core) were confirmed by a pathologist, and each point plotted represents the mean of a minimum of 4 independent fields of view (field diameter = 2mm) from margin and core (one section per mouse). The mean was calculated from 2 or 3 mice / experimental group.

Multiplex Immunohistochemistry (MxIHC) was performed on FFPE samples from the HNSCC cohort (Bulk RNA sequencing and analysis) (38), where tissue was available (n = 16; Research Ethics Committee reference 09/H0501/90). Staining and image processing was performed as previously with minor alterations (41). De-paraffinization, rehydration, antigen retrieval and IHC staining was performed using a Dako PT Link Autostainer and EnVision FLEX Target Retrieval Solution, High pH (Agilent Dako). The section was first stained with anti-Pan Cytokeratin (pre-diluted, Clone AE1/AE3; Agilent Dako), followed by biotinylated anti-Mouse IgG and Vectorstain elite ABC reagent (vector labs) as described above. Chromogenic visualization was completed with DAB and counterstaining with Haematoxylin. The staining was imaged using a Zeiss AxioScan.Z1 with 20x air immersion objective. Following this staining iteration, the section was sequentially stained as above, except using AEC for chromogenic visualization, with anti-αSMA, anti-GZMB and anti-CD8α (pre-diluted Kit IR62361-2; clone C8/144B; Agilent Dako) and scanned. Between each staining iteration, removal of the labile AEC staining (50% ethanol for 2 minutes; 100% ethanol for 2 minutes; 100% xylene for 2 minutes; 100% ethanol for 2 minutes; 50% ethanol for 2 minutes) and denaturation of the preceding antibodies through repeated antigen retrieval was performed. Image processing was performed in Fiji image analysis software. The PanCK alone image was used as a reference for registering each iteration of staining, using the linear stack alignment with SIFT Fiji plugin. Color deconvolution for Hematoxylin, DAB and AEC staining was performed using the Fiji plugin and images processed applying a positive staining threshold for each marker based on the initial (AEC negative) scan. Finally, processed images were combined to generate pseudo-IF multi-channel 8-bit TIFF images. Definiens Tissue Studio software (Definiens) was used to analyze the pseudo-IF multi-channel images for nuclear segmentation, cellular simulation and tumor boundary identification. CAFs were identified as α-SMA$^+$ PanCK- CD8- cells after excluding vessels using a machine learning classifier. Tumor center and margin regions were identified by a consultant pathologist (GJT). For comparing cell numbers across samples αSMA$^+$ CAFs or CD8$^+$ T-cells were quantified as the percentage of stromal/immune cells (non-epithelial PanCK-

cells) within each region. For distance measurements from CAFs to tumor cells 6 independent representative regions from within the tumor were selected by a consultant pathologist (GJT), and quantified as the average across all regions.

Immunocytochemistry. To visualize ECM, wells were decellularized with 0.25 M NH_4OH in 50 mM Tris buffer at 37°C for 30 minutes, washed in PBS and fixed with ice-cold 100% methanol at -20°C for 30 minutes and incubated with blocking solution containing PBS 1% BSA for 30 minutes. Collagen I primary antibody (abcam; 34710; 1:500) was applied for 1.5 hours. Secondary antibody anti-goat 488 (Invitrogen; 1:200) was applied for 45 minutes. To visualize cell associated proteins, cells were fixed in 4% paraformaldehyde solution and permeabilized in PBS containing 0.5% tritonX for 10 minutes. Cells were blocked with PBS 0.1% tritonX containing 2% BSA for 1.5 hours. αSMA primary antibody (Sigma Aldrich; 1A4; 1:100) was applied for 1 hour. Secondary antibody anti-mouse 546 (Invitrogen; 1:200) was added to cells for 45 minutes. DAPI was used as a counterstain to visualize cell nuclei (Invitrogen 1 in 1000) Fluorescence was visualized using an Olympus IX81 fluorescent microscope with Xcellence imaging software (Olympus). For ECM, a 4X objective was used with 3000 ms exposure time. For cells, a 20X objective was used with 1000 ms exposure for αSMA and 500 ms for DAPi. Mean fluorescence intensity of staining was calculated with Fiji software using the 'analyze' tool with the mean pixel intensity selected. Data was normalized to TGFβ1-treated positive control. Each point plotted represents the mean of 4 independent fields of view from one experimental condition. The mean was calculated from a minimum of 2 independent experiments.

Statistics. Statistical analyses were performed on a minimum of three independent experiments or biological replicates unless stated otherwise. Data are presented as mean $^+$ / - S.E.M. for all experiments. For normalized data where variance was equal to 0 for one group but significantly differed for the comparison group, Welch's correction was applied to the calculated *P* value. For tumor growth curves, statistical testing was performed on the mean

area under the curve (A.U.C) values for each curve. For cell proliferation curves, statistical tests were performed on the mean data from the final time point. Statistical tests were performed in GraphPad Prism v. 7. All statistical tests were two-sided and *P* values less than 0.05 were considered to be statistically significant. Significant values are marked with asterisks and represented the following: P≥0.05 (ns); ≤P<0.05(*); ≤P<0.01(**); 0.001≤P (***); P<0.0001(****).

Results

CAF suppress tumor responses to anti-cancer vaccination and αPD-1 immunotherapies.

We found that commonly used syngeneic murine tumors typically have low CAF content compared with human tumors. Immunostaining of $CAF^{mod/high}$ lung, colorectal and breast human tumors for αSMA [12, 15, 21] revealed that CAF content ranged from 15-60%. Comparatively, murine lung (TC1), colorectal (MC38) and breast (4T1) tumor models were CAF^{low} (<10%) (Fig. 1A). Therefore, we developed CAF-rich murine tumor models by co-injecting CAF with tumor cells, either by treating anatomically-matched fibroblasts with TGF-β1 (TC1, MC38) to produce cells with a typical myofibroblast CAF-like phenotype (upregulated *Acta2, Fn1, Col1A1*, *Col3A1*; αSMA-positive stress fibers; collagen I secretion; Supplementary Fig. S1A-C), or isolating CAF directly from BALB-neuT transgenic breast tumors (4T1; Supplementary Fig. S1A-C). This technique increased tumor growth (Supplementary Fig. S1D) and produced tumors with an αSMA-positive, CAF-rich stroma more typical of human cancers (Fig. 1B). Then we investigated whether CAF influenced tumor responses to different immunotherapies. First, we tested a vaccine model using HPV E6/E7-expressing TC1 cells [42]; mice were treated with DNA vaccine encoding the immunodominant CD8 epitope of HPV E7 (RAH, $E7_{49-57}$). Vaccination significantly reduced the volume of control tumors (3/8 mice showed complete tumor regression; Fig. 1C,D). No significant volume reduction was seen in CAF-rich tumors where all of the mice retained tumors (Fig. 1C,E). Next we explored whether CAF also promoted resistance to αPD-1 inhibition; treatment of mice with αPD-1 mAbs resulted in a significant reduction in MC38 [43] control tumor volume (4/8 mice had complete tumor regression; Fig. 1F,G). αPD-1 treatment did not significantly reduce volume of MC38 CAF-rich tumors where all of the mice retained tumors (Fig. 1F,H).

CAF exclude $CD8^+$ T-cells from tumors

To investigate the mechanism by which CAF promote immunotherapy resistance we first compared the immune cell composition of control and CAF-rich TC1 tumors using flow

cytometry; this showed that CAF-rich tumors contained more macrophages, but there were no significant differences in $CD8^+$ or $CD4^+$ T-cells (Fig. 2A). We used immunochemistry to examine the localization of immune cells in TC1, MC38 and 4T1 tumors; This showed that CAF markedly altered the distribution of $CD8^+$ T-cells which accumulated at the tumor periphery and were excluded from the tumor center (Fig. 2B & Supplementary Fig. S2A,B,C). CAF produced no change in $CD4^+$ T-cell localization. (Fig. 2C & Supplementary Fig. S2D,E) but did promote macrophage accumulation in and around the tumors (Fig. 2D & Supplementary Fig. S2F,G). Analysis of vaccine-treated TC1 tumors and αPD-1-treated MC38 tumors confirmed that CAF promoted $CD8^+$ T-cell exclusion from tumors (Supplementary Fig. S3A,B).

To examine the spatial and functional relationships between CAF and $CD8^+$ T-cells in human tumors we used multiplexed immunohistochemistry analysis (MxIHC; pan-cytokeratin [tumor cells], αSMA [CAF], CD8 and GZMB) of a cohort of head and neck cancers which had previously undergone RNA sequencing (Fig. 3A-C; 38). Initial analysis showed CAF^{high} tumors have significantly fewer $CD8^+$ T-cells in the center of the tumor compared to CAF^{low} tumors (Fig. 3C). In contrast, the number of CD8s at the margin of these tumors was not significantly different (Fig. 3C). To further examine the effect of CAFs on $CD8^+$ T-cells, we analyzed the relationships between spatial features and gene expression profiles. Weighted Gene Correlation Network Analysis (WGCNA) was used to identify correlated gene modules, which represent prominent biological processes activated in these samples (Supplementary Fig. S4A). This identified a module of genes involved in lymphocyte co-stimulation (GSEA: NES = 3.1, FDR Q = 0.003) which correlated with the density of $CD8^+$ tumor infiltrating lymphocytes (TILs; $r = 0.64$, $p = 0.01$; Supplementary Fig. S4B & Table S2). MxIHC staining showed $CD8^+$ T-cell exclusion in tumors where CAF directly abutted the tumor cells (i.e. low distance between CAF and tumor cells; Fig 3D). To quantify this observation, we measured the distance of CAF to tumor cells and examined how this related to expression of the lymphocyte co-stimulation module (summarized by the first principle component/eigengene). This showed a significant

correlation between lymphocyte co-stimulation eigengene expression and the distance of CAF to tumor cells (i.e. decreased co-stimulation where CAF directly abutted the tumor; Fig. 3E).

Upregulation of CTLA-4 in CD8$^+$ T-cells from CAF-rich tumors.

To investigate potential mechanisms promoting CD8$^+$ T-cell exclusion, we performed RNA sequencing on flow cytometry-sorted CD8$^+$ T-cells from CAF-rich and control TC1 tumors, (adjusted *P* value of <0.05 (DESeq2 analysis; Benjamini-Hochberg test, Fig. 4A & Table S)). One of the most highly upregulated genes was *Ctla4*, a CD28 homologue that acts as a negative regulator of T-cell response (44,45). Other upregulated genes included *Tnfrsf9* (41bb), a marker of antigen experience and *Irf4*, a transcription factor implicated in T-cell exhaustion. Gene set enrichment analysis (GSEA) of CD8$^+$ T-cells from CAF-rich versus CAF^{low} tumors significantly correlated with the *cytokine and cytotoxic* (NES 1.54, **P* = 0.02 Kolmogorov-Smirnov test) and *exhaustion* signatures (37) (NES 1.55, **P* = 0.05 Kolmogorov-Smirnov test; Fig. 4B). We used flow cytometry to examine CD8$^+$ T-cell exhaustion in CAF-rich tumors in further detail and confirmed increased expression of CTLA-4 (and TNFRSF9 and IRF4; Fig. 4C), but found no differences in expression of PD-1, granzyme B and Ki67 (Fig. 4D). Consistent with this finding, CD8$^+$ T-cells isolated from control and CAF-rich tumors following vaccination (E7 DNA vaccine) functioned similarly, with flow cytometry showing no differences in expression of IFNγ, TNFα or granzyme B effector cytokines following E7 peptide re-stimulation *ex vivo* (Fig. 4E).

Upregulation of CTLA-4 in the absence of additional 'classical' T-cell exhaustion markers, raised the possibility that CD8$^+$ T-cell exclusion could be mediated by CTLA-4 regulation of lymphocyte adhesion/migration (44,45). Analysis of human HNSCC (38) using multiplexed immunochemistry similarly showed that a proportion of excluded CD8$^+$ T-cells expressed CTLA-4 (range 5 - 34%; mean = 15.3%; Fig. 4F). Notably, inhibiting CTLA-4 in CAF-rich TC1 tumors using blocking (non-depleting) antibodies reduced tumor growth (Fig. 4G), decreased

$CD8^+$ T-cell exclusion (Fig. 4H; bottom panel) and increased infiltration (Fig. 3H; top panel). CTLA-4 blocking had no effect on intratumoral $FOXP3^+$ T-reg levels (Supplementary Fig. S4C) or growth of CAF-low TC1 tumors (Fig. 4G).

NOX4 inhibition promotes tumor $CD8^+$ T-cell infiltration.

Macrophages have been reported to promote T-cell exclusion from tumors, and therefore we investigated whether this was the case in our models [46]. Macrophage depletion using mAbs against CSF-1 however, did not affect tumor growth or $CD8^+$ T-cell distribution in CAF-rich TC1 tumors (Supplementary Fig. S4D-G). Next, we investigated whether targeting the CAF phenotype could promote $CD8^+$ T-cell infiltration into tumors. TGF-β1 regulates the myofibroblast-like CAF phenotype and we have shown previously that its downstream target, NOX4 regulates CAF differentiation in multiple human cancers (21). First, we tested the effect of TGF-β inhibition on CAF differentiation, phenotype and $CD8^+$ T-cell exclusion. In primary fibroblasts, TGF-β inhibition suppressed TGF-β1-induced myofibroblast differentiation (αSMA & collagen expression; Supplementary Fig. S5A-D) but had no effect on established CAF (Supplementary Fig. S5E-H). *In vivo*, TGF-β1 inhibition did not reduce intratumoral CAF levels (Supplementary Fig. S5I,J) or prevent $CD8^+$ T-cell exclusion (Supplementary Fig. S5K,L bottom panel). Despite this, TGF-β1 inhibition reduced the volume of CAF-rich TC1 and MC38 tumors (Supplementary Fig. 5M,N) and increased intratumoral $CD8^+$ T-cells (Supplementary Fig. S5K,L top panel). However, TGF-β1 inhibition similarly decreased tumor growth and increased $CD8^+$ T-cells in control (CAF^{low}) tumors (Supplementary Fig. S5O-R), suggesting the effect was CAF-independent.

The enzyme NOX4 generates intracellular ROS associated with myofibroblast differentiation (Supplementary Fig. S5A,B; S6A,B). Differentiated αSMA-positive CAF cultured *ex vivo* also showed increased ROS and NOX4 levels (Supplementary Fig. S6C,D). Similar to TGF-β1, the suppression of NOX4 activity using a NOX4/1 inhibitor (GKT137831 [Setanaxib]) suppressed

TGF-β1-induced myofibroblast differentiation (Supplementary Fig. S6E-H), but also 'normalised' fully differentiated CAF to a quiescent phenotype, downregulating expression of functional CAF markers, αSMA and collagen 1; Fig. 5A-D). Similar findings were observed using NOX4 shRNA (Supplementary Fig. S6I-L). *In vivo*, GKT137831 reduced CAF levels (Fig. 5E,F). The accumulation of $CD8^+$ T-cells at the tumor margin was no longer apparent and infiltration of $CD8^+$ T-cells cells into the tumor significantly increased (Fig. 5G,H) resulting in reduced tumor volume of CAF-rich TC1 and MC38 tumors (Fig. 5I,J). shNOX4 knockdown in CAF produced similar effects (Fig. 5K-M). GKT137831 had no effect on the growth of control (CAF^{low}) tumors (Supplementary Fig. S6M,N). Intriguingly, GKT137831 treatment also resulted in the re-expression of PD-L1 by MC38 cells, which was downregulated in CAF-rich tumors (Supplementary Fig. S6O).

NOX4 inhibition re-sensitises CAF-rich tumors to anti-cancer vaccination and αPD-1 checkpoint inhibition.

To investigate whether GKT137831 re-sensitized CAF-rich tumors to immunotherapy, mice with CAF-rich TC1 tumors were dosed with vaccine/GKT137831 combination. The combination treatment significantly reduced tumor volume (Fig. 6A), increased $CD8^+$ T-cell infiltration (Fig. 6B) and showed a non-significant trend for increased HPV-reactive $CD8^+$ T-cells (Fig. 6C). Although cessation of GKT137831 post-vaccine (day 31) resulted in tumor relapse (Fig. 6D), mice treated with the drug combination showed increased median survival (58 days vs 22 days) compared to vaccine monotherapy; Fig. 6E). Next we repeated the experiment, extending the duration of GKT137831 treatment and incorporating a second vaccine dose (Fig. 6F,G). Extending GKT137831 treatment following single vaccination partially prevented tumor relapse (2/7 mice relapsing compared to 5/8 mice in the group with earlier GKT137831 withdrawal; Fig. 6F) but did not significantly improve progression free survival (Fig. 6G). However, combining a second dose of vaccine with extended GKT137831 treatment resulted in long-term clearance of tumors in all mice (Fig. 6F,G).

Similarly, GKT137831 re-sensitized tumors to αPD-1 therapy; treatment of CAF-rich MC38 tumors with GKT137831/αPD-1 combination resulted in smaller tumors (Fig. 7A), higher tumor infiltration of $CD8^+$ T-cells (Fig. 7B) and increased overall survival compared to αPD-1 monotherapy (median survival 76.5 days [3/8 mice tumor-free] vs 39.5 days [1/8 mice tumor-free; Fig. 7C,D).

Discussion

Checkpoint immunotherapy is revolutionizing the treatment of a broad range of cancers, but a significant proportion of patients (~80%) fail to respond. There are many mechanisms by which tumors evade the immune system, including suppression of lymphocyte infiltration into the tumor mass. The 'immune excluded' phenotype is now recognized as a feature associated with poor response to checkpoint inhibition (10) and the identification of druggable mechanisms that regulate this effect could significantly improve clinical outcome. Here we show that CAF promote resistance to different immunotherapies by specifically excluding $CD8^+$ T-cells (but not $CD4^+$ T-cells) from the tumor mass, which then accumulate at the tumor margin. We found that CAF can be precisely targeted through the inhibition of NOX4 to both suppress and reverse CAF differentiation, thereby promoting intratumoral $CD8^+$ T-cell infiltration and re-sensitizing CAF-rich tumors to immunotherapy. Notably, we found that the excluded $CD8^+$ T-cells upregulate the expression of CTLA-4 in the absence of other exhaustion markers, and that the inhibition of CTLA-4 with blocking (non-depleting) antibodies also overcomes this exclusion effect.

Studies using single cell RNA sequencing have begun to characterize the CAF population in some detail, identifying specific CAF subpopulations with likely functional differences (47,48). Although the population is evidently heterogenous with no single marker identifying all CAF, the term CAF is used most commonly to describe a cell that phenotypically and functionally resembles a wound healing myofibroblast, albeit with some distinct characteristics; that is, a contractile, αSMA-positive cell that secretes collagen-rich ECM as well as numerous growth factors and cytokines (49,50). In contrast to myofibroblasts however, which during wound resolution either revert to a normal fibroblast or undergo apoptosis and elimination, CAF appear to be perpetually active (51). A significant proportion of most solid cancers are CAF-rich (including metastasis); for example, over 50% of cases of head and neck, esophageal,

colorectal and pancreatic cancers are dominated by the presence of CAF and these are associated with poor prognosis (21).

Recent analyses of melanoma and urothelial cancer patients treated with αPD-1/PD-L1 have identified non-response gene signatures that are characterized by prominent CAF ECM gene profiles (6,10). CAF can potentially promote tumor immune evasion through multiple potential mechanisms (52); CAF differentiation is TGF-β1-dependent, and CAF also amplify TGF-β1 signaling in tumors, promoting the secretion and activation of TGF-β1. This cytokine has numerous immunosuppressive effects such as inhibiting $CD8^+$ T-cell proliferation and cytotoxicity (53), and also induction of $CD8^+$ T-cell apoptosis through expression of PD-L2 and FasL (54). Therefore, TGF-β1 would seem an attractive target in CAF-rich tumors. Indeed, Mariathasan and colleagues have shown that TGF-β1 neutralizing mAbs promote a response to αPD-L1 therapy and facilitate lymphocyte infiltration into the tumor mass (10). TGF-β1, however, is a pleiotropic cytokine with both tumor-promoting and tumor-suppressive effects, and plays an important role in tissue homeostasis. Upstream targeting of the TGF-β pathway, therefore, is a potentially risky strategy. The use of small molecule TGF-β pathway inhibitors, for example, has been impeded by on-target toxicities, including cardiac effects and the development of cutaneous squamous cell carcinoma (55). In the present study, we found that treatment of CAF-rich tumors with a TGF-β1 inhibitor did not reduce CAF levels, or overcome $CD8^+$ T-cell exclusion, but did result in increased intratumoral CD8 T-cells. However, this response was also seen in control (CAF^{low}) tumors, suggesting that the effect was not mediated through CAF inhibition.

ECM proteins may also play a role in suppressing the response to immunotherapy. ECM production is a central CAF function, and CAF-rich tumors are often characterized by a desmoplastic stroma that is rich in collagen, fibronectin and various proteoglycans (hyaluronan, versican), which have been shown to 'trap' T-cells and inhibit T-cell motility (56). A dense

network of collagen fibers has also been shown to limit T-cell access to tumors (57) and enhance matrix density; the protease-independent nature of T-cell migration leads to contact guidance where T-cells follow a path-of-least-resistance along collagen fibers (58). Likewise, in fibrotic pancreatic cancers, T-cells accumulate in areas of low-density collagen (59,60). Therefore, drugs targeting ECM proteins such as hyaluronidase or LOXL2 inhibitors which suppress collagen cross linking, may have some utility for improving responses to immunotherapy. In the present study, *CTLA4* was one of the most upregulated genes in the excluded $CD8^+$ T-cells from CAF-rich tumors (in the absence of other exhaustion markers or evidence of suppressed activity). Although CTLA-4 classically negatively regulates T-cell function, it has also been shown to promote T-cell adhesion and suppresses migration by modulating integrin activation (44,45). αCTLA-4 antibodies have been shown to enhance T-cell motility and overcome matrix-dependent stop signals (61). Similarly we found that blocking CTLA-4 with non-depleting antibodies promoted $CD8^+$ T-cell tumor infiltration (sparing T-regs), suggesting that CTLA-4 targeting could also have benefit in CAF-rich tumors, and perhaps contributes to the increased efficacy of αPD-1/αCTLA-4 combinations (62).

In the past, attempts to therapeutically target CAF have been unsuccessful and, possibly compounded by poor understanding of CAF heterogeneity and lack of specific CAF targets. Depletion of fibroblast activation protein (FAP)-positive CAF in murine models enhances anti-tumor immunity (63) but clinically targeting FAP in colorectal cancer was not successful (19,20). Furthermore, FAP expression has been identified on bone marrow stem cells and therefore off-target effects resulting from FAP-targeting cannot be excluded (64). Hedgehog inhibition has also been used to target CAF effectively in preclinical models (65) but has produced disappointing results in phase II clinical testing in metastatic pancreatic cancer (18-20). Recently, Chen and colleagues pharmacologically inhibited CXCR4 using Plerixafor in murine models of breast cancer and demonstrated that the decreased fibrosis increased T-cell infiltration and improved response to checkpoint inhibition (65). CXCR4 is expressed on a wide

variety of immune cells, including T-cells, B-cells and hematopoietic stem cells, and has been shown to promote αPD-1 response through inhibition of myeloid derived suppressor cells (65).

We have shown previously that NOX4, a ROS-producing enzyme and downstream target of TGF-β1, promotes CAF activation in human cancers and is relatively CAF-specific (21). GKT137831 (Setanaxib) is an orally available, small organic molecule of the pyrazolopyridine dione chemical class; it is a selective inhibitor of NOX4/1 and the first drug in this class of NOX inhibitors to enter the clinic (phase II clinical testing treating fibrotic disease (liver, kidney, lung fibrosis; NCT03226067, NCT02010242 respectively). In the present study, we found that GKT137831 not only prevents CAF differentiation, but 'normalizes' established CAF to a more quiescent fibroblast-like cell, downregulating classical CAF markers such as αSMA and ECM proteins. These findings suggest and that CAF are not fixed in a terminally differentiated state, but require continuous NOX4-dependent ROS generation to maintain their phenotype. CAF can therefore be specifically targeted with GKT137831 to reshape the CAF-regulated immune microenvironment.

In summary, CAF-rich tumors respond poorly to αPD-1/PD-L1 immunotherapy and currently there are no pharmacological means of targeting this cell-type specifically (6,10). The results of the present study show that CAF-mediated immunotherapy resistance results from the exclusion of $CD8^+$ T-cells from the tumor mass. This phenomenon can be successfully overcome by reversing the CAF phenotype through NOX4 inhibition using GKT137831 (Setanaxib), a clinically tested drug with an excellent safety profile. A significant proportion of solid cancers are CAF-rich, and our data suggest that the combination of NOX4 inhibition and immunotherapy would improve clinical outcome in these tumors.

References

1. Topalian SL, Drake CG, Pardoll DM. Immune checkpoint blockade: a common denominator approach to cancer therapy. Cancer cell **2015**;27:450-61
2. Robert C, Long GV, Brady B, Dutriaux C, Maio M, Mortier L*, et al.* Nivolumab in Previously Untreated Melanoma without BRAF Mutation. New England Journal of Medicine **2014**;372:320-30
3. Ran X, Yang K. Inhibitors of the PD-1/PD-L1 axis for the treatment of head and neck cancer: current status and future perspectives. Drug Design, Development and Therapy **2017**;11:2007-14
4. Hu Z, Ott PA, Wu CJ. Towards personalized, tumor-specific, therapeutic vaccines for cancer. Nature reviews Immunology **2018**;18:168-82
5. Chen L, Han X. Anti–PD-1/PD-L1 therapy of human cancer: past, present, and future. The Journal of Clinical Investigation **2015**;125:3384-91
6. Hugo W, Zaretsky JM, Sun L, Song C, Moreno BH, Hu-Lieskovan S*, et al.* Genomic and Transcriptomic Features of Response to Anti-PD-1 Therapy in Metastatic Melanoma. Cell **2016**;165:35-44
7. Tumeh PC, Harview CL, Yearley JH, Shintaku IP, Taylor EJ, Robert L*, et al.* PD-1 blockade induces responses by inhibiting adaptive immune resistance. Nature **2014**;515:568-71
8. Herbst RS, Soria JC, Kowanetz M, Fine GD, Hamid O, Gordon MS*, et al.* Predictive correlates of response to the anti-PD-L1 antibody MPDL3280A in cancer patients. Nature **2014**;515:563-7
9. Jiang P, Gu S, Pan D, Fu J, Sahu A, Hu X*, et al.* Signatures of T cell dysfunction and exclusion predict cancer immunotherapy response. Nature medicine **2018**
10. Mariathasan S, Turley SJ, Nickles D, Castiglioni A, Yuen K, Wang Y*, et al.* TGFbeta attenuates tumor response to PD-L1 blockade by contributing to exclusion of T cells. Nature **2018**;554:544-8
11. Ascierto ML, Makohon-Moore A, Lipson EJ, Taube JM, McMiller TL, Berger AE*, et al.* Transcriptional Mechanisms of Resistance to Anti-PD-1 Therapy. Clinical cancer research **2017**;23:3168-80
12. Marsh D, Suchak K, Moutasim KA, Vallath S, Hopper C, Jerjes W*, et al.* Stromal features are predictive of disease mortality in oral cancer patients. J Pathol **2011**;223:470-81
13. Parikh JG, Kulkarni A, Johns C. alpha-smooth muscle actin-positive fibroblasts correlate with poor survival in hepatocellular carcinoma. Oncology letters **2014**;7:573-5
14. Sinn M, Denkert C, Striefler JK, Pelzer U, Stieler JM, Bahra M*, et al.* [alpha]-Smooth muscle actin expression and desmoplastic stromal reaction in pancreatic cancer: results from the CONKO-001 study. Br J Cancer **2014**;111:1917-23
15. Underwood TJ, Hayden AL, Derouet M, Garcia E, Noble F, White MJ*, et al.* Cancer-associated fibroblasts predict poor outcome and promote periostin-dependent invasion in oesophageal adenocarcinoma. The Journal of Pathology **2015**;235:466-77
16. Hanahan D, Weinberg RA. Hallmarks of cancer: the next generation. Cell **2011**;144:646-74
17. Chakravarthy A, Khan L, Bensler NP, Bose P, De Carvalho DD. TGF-beta-associated extracellular matrix genes link cancer-associated fibroblasts to immune evasion and immunotherapy failure. Nature communications **2018**;9:4692
18. Catenacci DV, Junttila MR, Karrison T, Bahary N, Horiba MN, Nattam SR*, et al.* Randomized Phase Ib/II Study of Gemcitabine Plus Placebo or Vismodegib, a Hedgehog Pathway Inhibitor, in Patients With Metastatic Pancreatic Cancer. Journal of clinical oncology : official journal of the American Society of Clinical Oncology **2015**;33:4284-92

19. Hofheinz RD, al-Batran SE, Hartmann F, Hartung G, Jager D, Renner C*, et al.* Stromal antigen targeting by a humanised monoclonal antibody: an early phase II trial of sibrotuzumab in patients with metastatic colorectal cancer. Onkologie **2003**;26:44-8
20. Narra K, Mullins SR, Lee HO, Strzemkowski-Brun B, Magalong K, Christiansen VJ*, et al.* Phase II trial of single agent Val-boroPro (Talabostat) inhibiting Fibroblast Activation Protein in patients with metastatic colorectal cancer. Cancer biology & therapy **2007**;6:1691-9
21. Hanley CJ, Mellone M, Ford K, Thirdborough SM, Mellows T, Frampton SJ*, et al.* Targeting the Myofibroblastic Cancer-Associated Fibroblast Phenotype Through Inhibition of NOX4. Journal of the National Cancer Institute **2018**;110
22. Lin KY, Guarnieri FG, Staveley-O'Carroll KF, Levitsky HI, August JT, Pardoll DM*, et al.* Treatment of established tumors with a novel vaccine that enhances major histocompatibility class II presentation of tumor antigen. Cancer research **1996**;56:21-6
23. Corbett TH, Griswold DP, Jr., Roberts BJ, Peckham JC, Schabel FM, Jr. Tumor induction relationships in development of transplantable cancers of the colon in mice for chemotherapy assays, with a note on carcinogen structure. Cancer research **1975**;35:2434-9
24. Aslakson CJ, Miller FR. Selective events in the metastatic process defined by analysis of the sequential dissemination of subpopulations of a mouse mammary tumor. Cancer research **1992**;52:1399-405
25. Chotprakaikiat W, Allen A, Bui-Minh D, Harden E, Jobsri J, Cavallo F*, et al.* A plant-expressed conjugate vaccine breaks CD4(+) tolerance and induces potent immunity against metastatic Her2(+) breast cancer. Oncoimmunology **2016**;5:e1166323-e
26. Rice J, Buchan S, Stevenson FK. Critical components of a DNA fusion vaccine able to induce protective cytotoxic T cells against a single epitope of a tumor antigen. Journal of immunology (Baltimore, Md : 1950) **2002**;169:3908-13
27. Allen A, Wang C, Caproni LJ, Sugiyarto G, Harden E, Douglas LR*, et al.* Linear doggybone DNA vaccine induces similar immunological responses to conventional plasmid DNA independently of immune recognition by TLR9 in a pre-clinical model. Cancer immunology, immunotherapy : CII **2018**;67:627-38
28. Engel I, Seumois G, Chavez L, Samaniego-Castruita D, White B, Chawla A*, et al.* Innate-like functions of natural killer T cell subsets result from highly divergent gene programs. Nature immunology **2016**;17:728-39
29. Picelli S, Faridani OR, Bjorklund AK, Winberg G, Sagasser S, Sandberg R. Full-length RNA-seq from single cells using Smart-seq2. Nature protocols **2014**;9:171-81
30. Trapnell C, Pachter L, Salzberg SL. TopHat: discovering splice junctions with RNA-Seq. Bioinformatics (Oxford, England) **2009**;25:1105-11
31. Langmead B, Trapnell C, Pop M, Salzberg SL. Ultrafast and memory-efficient alignment of short DNA sequences to the human genome. Genome biology **2009**;10:R25
32. Li H, Durbin R. Fast and accurate short read alignment with Burrows-Wheeler transform. Bioinformatics (Oxford, England) **2009**;25:1754-60
33. Anders S, Pyl PT, Huber W. HTSeq--a Python framework to work with high-throughput sequencing data. Bioinformatics (Oxford, England) **2015**;31:166-9
34. Love MI, Huber W, Anders S. Moderated estimation of fold change and dispersion for RNA-seq data with DESeq2. Genome biology **2014**;15:550
35. Ganesan AP, Clarke J, Wood O, Garrido-Martin EM, Chee SJ, Mellows T*, et al.* Tissue-resident memory features are linked to the magnitude of cytotoxic T cell responses in human lung cancer. Nature immunology **2017**;18:940-50
36. Patil VS, Madrigal A, Schmiedel BJ, Clarke J, O'Rourke P, de Silva AD*, et al.* Precursors of human CD4(+) cytotoxic T lymphocytes identified by single-cell transcriptome analysis. Science immunology **2018**; 3(19): pii: eaan8664.
37. Best JA, Blair DA, Knell J, Yang E, Mayya V, Doedens A*, et al.* Transcriptional insights into the CD8(+) T cell response to infection and memory T cell formation. Nature immunology **2013**;14:404-12

38. Wood O, Clarke J, Woo J, Mirza AH, Woelk CH, Thomas GJ*, et al.* Head and Neck Squamous Cell Carcinomas Are Characterized by a Stable Immune Signature Within the Primary Tumor Over Time and Space. Clinical cancer research : an official journal of the American Association for Cancer Research **2017**;23:7641-9
39. Langfelder P, Horvath S. WGCNA: an R package for weighted correlation network analysis. BMC bioinformatics **2008**;9:559
40. Ritchie ME, Phipson B, Wu D, Hu Y, Law CW, Shi W*, et al.* limma powers differential expression analyses for RNA-sequencing and microarray studies. Nucleic acids research **2015**;43:e47
41. Remark R, Merghoub T, Grabe N, Litjens G, Damotte D, Wolchok JD*, et al.* In-depth tissue profiling using multiplexed immunohistochemical consecutive staining on single slide. Science immunology **2016**;1:aaf6925
42. Ottensmeier CH, Perry KL, Harden EL, Stasakova J, Jenei V, Fleming J*, et al.* Upregulated Glucose Metabolism Correlates Inversely with CD8+ T-cell Infiltration and Survival in Squamous Cell Carcinoma. Cancer research **2016**;76:4136-48
43. Mosely SI, Prime JE, Sainson RC, Koopmann JO, Wang DY, Greenawalt DM*, et al.* Rational Selection of Syngeneic Preclinical Tumor Models for Immunotherapeutic Drug Discovery. Cancer immunology research **2017**;5:29-41
44. Schneider H, Valk E, da Rocha Dias S, Wei B, Rudd CE. CTLA-4 up-regulation of lymphocyte function-associated antigen 1 adhesion and clustering as an alternate basis for coreceptor function. Proceedings of the National Academy of Sciences of the United States of America **2005**;102:12861-6
45. Zell T, Warden CS, Chan AS, Cook ME, Dell CL, Hunt SW, 3rd*, et al.* Regulation of beta 1-integrin-mediated cell adhesion by the Cbl adaptor protein. Current biology : CB **1998**;8:814-22
46. Peranzoni E, Lemoine J, Vimeux L, Feuillet V, Barrin S, Kantari-Mimoun C*, et al.* Macrophages impede CD8 T cells from reaching tumor cells and limit the efficacy of anti-PD-1 treatment. Proceedings of the National Academy of Sciences of the United States of America **2018**;115:E4041-e50
47. Lambrechts D, Wauters E, Boeckx B, Aibar S, Nittner D, Burton O*, et al.* Phenotype molding of stromal cells in the lung tumor microenvironment. Nature medicine **2018**;24:1277-89
48. Puram SV, Tirosh I, Parikh AS, Patel AP, Yizhak K, Gillespie S*, et al.* Single-Cell Transcriptomic Analysis of Primary and Metastatic Tumor Ecosystems in Head and Neck Cancer. Cell **2017**;171:1611-24.e24
49. Chang HY, Sneddon JB, Alizadeh AA, Sood R, West RB, Montgomery K*, et al.* Gene expression signature of fibroblast serum response predicts human cancer progression: similarities between tumors and wounds. PLoS biology **2004**;2:E7
50. Darby IA, Zakuan N, Billet F, Desmouliere A. The myofibroblast, a key cell in normal and pathological tissue repair. Cellular and molecular life sciences : CMLS **2016**;73:1145-57
51. Li H, Fan X, Houghton J. Tumor microenvironment: the role of the tumor stroma in cancer. Journal of cellular biochemistry **2007**;101:805-15
52. Ziani L, Chouaib S, Thiery J. Alteration of the Antitumor Immune Response by Cancer-Associated Fibroblasts. Frontiers in immunology **2018**;9:414-
53. Li MO, Flavell RA. TGF-beta: a master of all T cell trades. Cell **2008**;134:392-404
54. Lakins MA, Ghorani E, Munir H, Martins CP, Shields JD. Cancer-associated fibroblasts induce antigen-specific deletion of CD8 (+) T Cells to protect tumor cells. Nature communications **2018**;9:948
55. de Gramont A, Faivre S, Raymond E. Novel TGF-β inhibitors ready for prime time in onco-immunology. Oncoimmunology **2016**;6:e1257453-e
56. Evanko SP, Potter-Perigo S, Bollyky PL, Nepom GT, Wight TN. Hyaluronan and versican in the control of human T-lymphocyte adhesion and migration. Matrix biology : journal of the International Society for Matrix Biology **2012**;31:90-100

57. Salmon H, Franciszkiewicz K, Damotte D, Dieu-Nosjean MC, Validire P, Trautmann A*, et al.* Matrix architecture defines the preferential localization and migration of T cells into the stroma of human lung tumors. J Clin Invest **2012**;122:899-910
58. Bougherara H, Mansuet-Lupo A, Alifano M, Ngo C, Damotte D, Le Frere-Belda MA*, et al.* Real-Time Imaging of Resident T Cells in Human Lung and Ovarian Carcinomas Reveals How Different Tumor Microenvironments Control T Lymphocyte Migration. Frontiers in immunology **2015**;6:500
59. Ene-Obong A, Clear AJ, Watt J, Wang J, Fatah R, Riches JC*, et al.* Activated pancreatic stellate cells sequester CD8+ T cells to reduce their infiltration of the juxtatumoral compartment of pancreatic ductal adenocarcinoma. Gastroenterology **2013**;145:1121-32
60. Hartmann N, Giese NA, Giese T, Poschke I, Offringa R, Werner J*, et al.* Prevailing role of contact guidance in intrastromal T-cell trapping in human pancreatic cancer. Clinical cancer research : an official journal of the American Association for Cancer Research **2014**;20:3422-33
61. Ruocco MG, Pilones KA, Kawashima N, Cammer M, Huang J, Babb JS*, et al.* Suppressing T cell motility induced by anti-CTLA-4 monotherapy improves antitumor effects. J Clin Invest **2012**;122:3718-30
62. Larkin J, Hodi FS, Wolchok JD. Combined Nivolumab and Ipilimumab or Monotherapy in Untreated Melanoma. N Engl J Med **2015**;373:1270-1
63. Kraman M, Bambrough PJ, Arnold JN, Roberts EW, Magiera L, Jones JO*, et al.* Suppression of antitumor immunity by stromal cells expressing fibroblast activation protein-alpha. Science (New York, NY) **2010**;330:827-30
64. Tran E, Chinnasamy D, Yu Z, Morgan RA, Lee CC, Restifo NP*, et al.* Immune targeting of fibroblast activation protein triggers recognition of multipotent bone marrow stromal cells and cachexia. The Journal of Experimental Medicine **2013**;210:1125-35
65. Olive KP, Jacobetz MA, Davidson CJ, Gopinathan A, McIntyre D, Honess D*, et al.* Inhibition of Hedgehog signaling enhances delivery of chemotherapy in a mouse model of pancreatic cancer. Science (New York, NY) **2009**;324:1457-61

Figure legends

Fig. 1 – CAF suppress response to anti-cancer vaccination and αPD-1 immunotherapy.

A) IHC for αSMA showing CAF content in murine and human tumors. Representative αSMA images, scale bar = 100 *μ*m; area % of staining was quantified in human and murine lung, colorectal and breast tumors (human n=9 per group; murine 7-10 per group; mean +/- s.e.m; **P* < 0.05, *****P* < 0.0001 One-Way ANOVA test). **B)** IHC showing αSMA+ CAF content in tumors with CAF co-injection; TC1, MC38 and 4T1 tumors respectively. Representative images from αSMA IHC are shown; scale bar = 50 μm (TC1), 100 μm (MC38, 4T1); area % of staining was quantified (mean +/- s.e.m, **P* < 0.05, ***P* < 0.01 two-tailed *t* test). **C)** TC1 tumor growth curves showing effect of CAF on response to HPV E7 vaccination (control tumors – red; CAF-rich tumors- blue). Control vaccine groups tumors are shown in black and grey respectively (mean +/- s.e.m., from n = 7 - 8 mice per group, ns > 0.05, **P* < 0.05 AUC analysis followed by two-tailed *t* test. **D,E)** Tumor growth curves from individual mice following HPV E7 vaccination (control tumors – red; CAF-rich tumors- blue respectively). **F)** MC38 tumor growth curves showing the effect of CAF on response to αPD-1 therapy (control tumors – blue; CAF-rich tumors- orange). Isotype control antibody-treated tumors are shown in black and grey respectively (mean +/- s.e.m., from n = 8 mice per group, ns > 0.05, **P* < 0.05 AUC analysis followed by two-tailed *t* test). **G,H)** Tumor growth curves from individual mice following αPD-1 antibody treatment (control tumors – blue; CAF-rich tumors – orange respectively).

Fig. 2 – CAF exclude CD8+ T-cells from tumors.

A) Flow cytometry analysis of CD8+ T-cell, CD4+ T-cell and macrophage infiltration in disaggregated TC1 control (CAF^{low}) and CAF-rich tumors, gating on CD8+, CD4+ and CD11b+ F480+ respectably from CD45+ viable singlets (mean +/- s.e.m., n = 4 tumors per group, ns > 0.05, **P* < 0.05, two-tailed *t* test). **B,C,D)** IHC on TC1 tumors showing the effect of on spatial distribution of CD8+ T-cells **(B),** CD4+ T-cells **(C)** and macrophages **(D)** at the tumor center/margin. Representative images are shown from tumor center (top panel) and margin

(bottom panel). Scale bars = 100 μm and % staining area was quantified (mean +/- s.e.m., *$P <$ 0.05, two-tailed *t* test).

Fig. 3 - Analysis of CAF and CD8$^+$ T-cell spatial relationship in human head and neck cancers. A) Representative images of MxIHC staining in CAF^{high} and CAF^{low} tumors from the center and margin. **B,C**) Quantification of αSMA$^+$ (B) and CD8$^+$ (C) cells as a proportion of stromal/immune cells (non-epithelial PanCK- cells) at the tumor center or margin in CAF^{high} and CAF^{low} tumors. Plots show each independent data point (different patient samples) plus the mean and s.e.m., statistical comparisons are made using an ordinary one-way ANOVA multiple comparisons test. **D)** Representative images of MxIHC staining of a tumor where CAFs directly abutted the tumor and where CAFs are distant from the tumor border. **E)** Scatter plot showing the relationship between the WGCNA lymphocyte co-stimulation module eigengene and histo-cytometry measurements of the median distance between CAF and the nearest tumor cell. Pearson's r and associated p values are shown. Scale bars represent 100μm.

.

Fig. 4 – CD8$^+$ T-cells in CAF-rich tumors upregulate CTLA-4. A) RNA-Seq analysis of differentially expressed genes (one per row) by CD8$^+$ T-cells from TC1 control *versus* TC1 CAF-rich tumors (n = 4 mice per group) (adjusted *P* value of <0.05 (DESeq2 analysis; Benjamini-Hochberg test)), presented as row-wise *z*-scores of transcripts per million (TPM); each column represents an individual sample; right margin, examples of DEGs (vertical line groups genes upregulated in CD8$^+$ T-cells in TC1 CAF-rich tumors relative to their expression in TC1 control tumors). **B)** GSEA of various gene sets (above plots) in the transcriptome of CD8$^+$ T-cells from TC1 CAF-rich *versus* TC1 control tumors: top, running enrichment score (RES) for the gene set, from most enriched at the left to most under-represented at the right; middle, positions of gene set members (blue vertical lines) in the ranked list of genes; bottom, value of the ranking metric. Values above the plot represent the normalized enrichment score

(NES) and *P* values, Kolmogorov-Smirnov test. **C)** Flow cytometry analysis of CTLA-4, IRF4 and TNFRSF9 (4-1bb) expression in $CD8^+$ T-cells from TC1 control (CAF^{low}) and TC1 CAF-rich tumors (left and right plots respectively; mean +/- s.e.m., from n = 6 mice per group, $*P < 0.05$, $**P < 0.01$ two-tailed *t* test). **D)** Flow cytometry analysis of PD-1, granzyme B and ki67 in $CD8^+$ T-cells from TC1 control (CAF^{low}) and TC1 CAF-rich tumors (left and right plots respectively; mean +/- s.e.m., from n = 6 mice per group, ns > 0.05 two-tailed *t* test). **E)** Analysis of cytokine expression in $CD8^+$ T-cells isolated from E7 vaccinated TC1 control and CAF-rich tumors following peptide re-stimulation *ex vivo*. Example flow cytometry plots are shown from CAF-rich tumors with quantification, gating $CD8^+$ cells expressing IFNy, TNFα and granzyme B from isotype controls (mean +/- s.e.m., from n = 8 mice per group, ns > 0.05 two-tailed *t* test). **F)** Representative images from multiplexed IHC and histo-cytometry analysis of CTLA-4 expression on excluded $CD8^+$ T-cells at the periphery of human HNSCC tumors (n= 7). i) Micrograph from tumor margin, showing Pan-Cytokeratin (PanCK; brown) and hematoxylin (blue) staining, scale bar represents 1mm. ii) Point Pattern plot (for the region shown in i), showing the slide position of cells identified through histo-cytometry analysis: each point represents the centroid of a cell, colored by classification shown in key below. iii) Micrograph showing a pseudo-coloured micrograph showing staining for PanCK, CD8 and CTLA-4 (as shown in the adjacent 'single channel' panels), in the region of interest (ROI) highlighted by the rectangle in ii. Scale bar represents 100µm. **G)** Tumor growth curves showing the effect of αCTLA-4 mAb treatment on CAF-rich and CAF-low TC1 tumors (mean +/- s.e.m., from n = 5 mice per group, ns > 0.05, *P < 0.05, AUC analysis followed by two-tailed t test. **H)** IHC showing $CD8^+$ T-cell spatial distribution in TC1 CAF-rich tumors following treatment with αCTLA-4 mAb or isotype control mAb (tumor center [top panel]; tumor margin [bottom panel]), scale bars = 100 µm. Area % of staining is quantified (mean +/- s.e.m., ns > 0.05, *P < 0.05, two-tailed t test).

Fig. 5 - NOX4 inhibition reverses the CAF phenotype and promotes $CD8^+$ T-cell infiltration.

A-D) Effect of NOX4 inhibition (GKT137831) on established BALBneuT breast CAF. **A)** Q-PCR analysis of NOX4 gene expression. **B)** Intracellular ROS analysis. **C,D)**, Immunofluorescence showing αSMA stress fiber formation (red; **C**) and collagen I (green; **D**). Representative images are shown; scale bars = 50 μm and 200 μm respectively and mean fluorescence intensity was quantified (all data represents mean +/- s.e.m, from 2 or 3 independent experiments, $*P < 0.05$ two-tailed *t* test with Welch's correction). **E,F)** IHC for αSMA showing the effect of GKT137831 treatment on CAF content in TC1 CAF-rich and MC38 CAF-rich tumors respectively. Representative images are shown, scale bar = 100 μm and area % of staining was quantified (mean +/- s.e.m, $*P < 0.05$ two-tailed *t* test). **G,H)** IHC showing the effect of GKT137831 treatment on $CD8^+$ T-cell spatial distribution in TC1 CAF-rich and MC38 CAF-rich tumors respectively. Representative images are shown from tumor center (top panel) and margin (bottom panel). Scale bars = 100 μm and % staining area was quantified (mean +/- s.e.m, $*P < 0.05$ two-tailed *t* test). **I,J)** Tumor growth curves showing the effect of GKT137831 treatment on TC1 CAF-rich and MC38 CAF-rich tumors respectively (mean +/- s.e.m., from n = 6 - 7 mice per group, $*P < 0.05$, $**P < 0.01$ AUC analysis followed by two-tailed *t* test. **K)** Tumor growth curves showing effect of CAF shRNA NOX4 knockdown on the growth of TC1 CAF-rich tumors (mean +/- s.e.m., from n = 8 mice per group, $**P < 0.01$ AUC analysis followed by two-tailed *t* test. **L, M)** IHC showing the effect of CAF shRNA NOX4 knockdown on αSMA expression **(L)** and $CD8^+$ T-cell infiltration **(M)** in TC1 CAF-rich tumors Representative images are shown from tumor center (top panel) and margin (bottom panel). Scale bars = 50 μm and 100 μm respectively, and % staining area was quantified (mean +/- s.e.m, $*P < 0.05$, $**P < 0.01$, $P < 0.001$ two-tailed *t* test).

Fig. 6 – NOX4 inhibition promotes CD8+ T-cell infiltration and re-sensitises CAF-rich tumors to anti-HPV E7 vaccination. A) Tumor growth curves of TC1 CAF-rich tumors showing the effect of HPV E7 vaccine (blue), GKT137831 (grey) and combination (purple) treatments; control tumors are shown in black (mean +/- s.e.m., from n = 10 mice per group, *P

< 0.05 AUC analysis followed by two-tailed *t* test. **B)** IHC showing the effect of vaccine vs vaccine/GKT137831 on $CD8^+$ T-cell infiltration in TC1 CAF-rich tumors. Representative images are shown from tumor center (top panel) and margin (bottom panel). Scale bars = 100 μm and % staining area was quantified (mean +/- s.e.m, $*P < 0.05$, $**P < 0.01$ two-tailed *t* test). **C)** Flow cytometry analysis of % $CD8^+$ E7 $tetramer^+$ staining in control, vaccine, GKT137831 and vaccine/GKT137831 treated tumors, gated from $CD45^+$ viable single cells (mean +/- s.e.m., n = 8 mice per group), ns > 0.05, two-tailed t test). **D)** Tumor growth curves of TC1 CAF-rich tumors showing relapse following withdrawal of GKT137831 at day 31. Individual mouse tumor volume measurements are shown from vaccine monotherapy (blue) and combination (purple) n = 6 mice per group. Dotted line represents when GKT137831 was stopped. **(E)** Kaplan-Meier survival curves showing effect of HPV E7 vaccine (blue), GKT137831 (grey) and combination (purple); control mice are shown in black (n=6 mice per group $*P < 0.05$ Log-rank (Mantel-Cox) test). **F,G)** Tumor growth curves **(F)** and Kaplan-Meier analysis **(G)** of TC1 CAF-rich tumors showing the effect of single dose HPV E7 vaccination combined with either short-term or long-term treatment with GKT137831 (black and grey respectively); long-term GKT137831 treatment was also tested in combination with a second dose of HPV E7 vaccination administered following initial response (purple). Individual mouse tumor volume measurements are shown; GKT137831 removed (black), continued GKT137831 only (grey) and continued GKT137831 + additional vaccine (purple) n = 7-8 mice per group, $**P < 0.01$ Log-rank (Mantel-Cox) test).

Fig. 7 – NOX4 inhibition re-sensitizes CAF-rich tumors to anti-PD-1 checkpoint therapy

A) Tumor growth curves of MC38 CAF-rich tumors showing the effect of αPD-1 (orange), GKT137831 (grey) and combination (blue) assessed by tumor volume measurements; control tumors are shown in black (mean +/- s.e.m., from n = 11 mice per group, $*P < 0.05$ AUC analysis followed by two-tailed *t* test. **B)** IHC showing the effect of αPD-1 vs αPD-1/GKT137831 on $CD8^+$ T-cell infiltration in MC381 CAF-rich tumors. Representative images are shown from tumor center (top panel) and margin (bottom panel). Scale bars = 100 μm and %

staining area was quantified (mean +/- s.e.m, *$P < 0.05$ two-tailed *t* test. **C)** Growth curves showing individual mouse tumor volume measurements of CAF-rich MC38 tumor growth following αPD-1 treatment (orange) or αPD-1 + GKT137831 treatment (blue) n = 8 mice per group. **D)** Kaplan-Meier survival curves showing effect of αPD-1 (orange), GKT137831 (grey) and combination (blue) in CAF-rich MC38 tumors; control mice are shown in black (n = 8 mice / group *$P < 0.05$ Log-rank (Mantel-Cox) test).

Figure 1

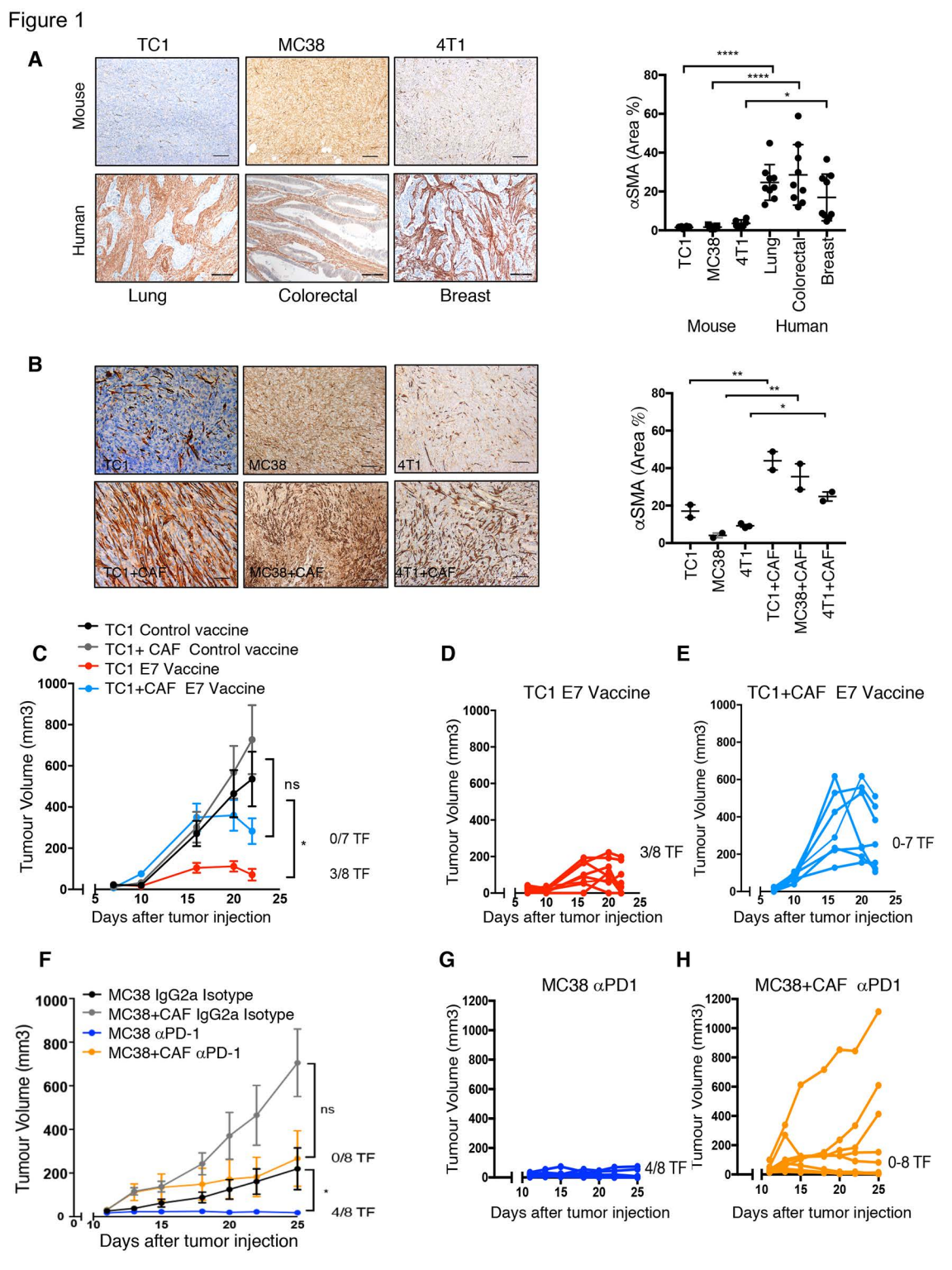
A
TC1
MC38
4T1
Mouse
Human
Lung
Colorectal
Breast
αSMA (Area %)
TC1
MC38
4T1
Lung
Colorectal
Breast
Mouse
Human
B
TC1
MC38
4T1
TC1+CAF
MC38+CAF
4T1+CAF
αSMA (Area %)
C
TC1 Control vaccine
TC1+ CAF Control vaccine
TC1 E7 Vaccine
TC1+CAF E7 Vaccine
Tumour Volume (mm3)
Days after tumor injection
ns
0/7 TF
3/8 TF
D
TC1 E7 Vaccine
3/8 TF
E
TC1+CAF E7 Vaccine
0-7 TF
F
MC38 IgG2a Isotype
MC38+CAF IgG2a Isotype
MC38 αPD-1
MC38+CAF αPD-1
ns
0/8 TF
4/8 TF
G
MC38 αPD1
4/8 TF
H
MC38+CAF αPD1
0-8 TF

Figure 2

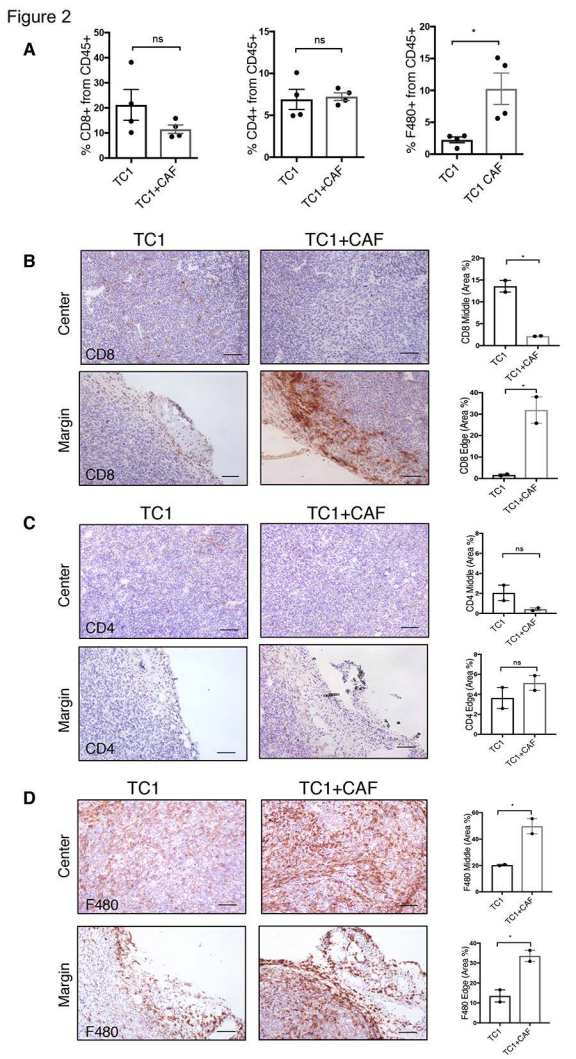
A
% CD8+ from CD45+
ns
TC1
TC1+CAF
% CD4+ from CD45+
ns
TC1
TC1+CAF
% F480+ from CD45+
*
TC1
TC1 CAF
B
TC1
TC1+CAF
Center
CD8
Margin
CD8
CD8 Middle (Area %)
*
TC1
TC1+CAF
CD8 Edge (Area %)
*
TC1
TC1+CAF
C
TC1
TC1+CAF
Center
CD4
Margin
CD4
CD4 Middle (Area %)
ns
TC1
TC1+CAF
CD4 Edge (Area %)
ns
TC1
TC1+CAF
D
TC1
TC1+CAF
Center
F480
Margin
F480
F480 Middle (Area %)
*
TC1
TC1+CAF
F480 Edge (Area %)
*
TC1
TC1+CAF

Figure 3

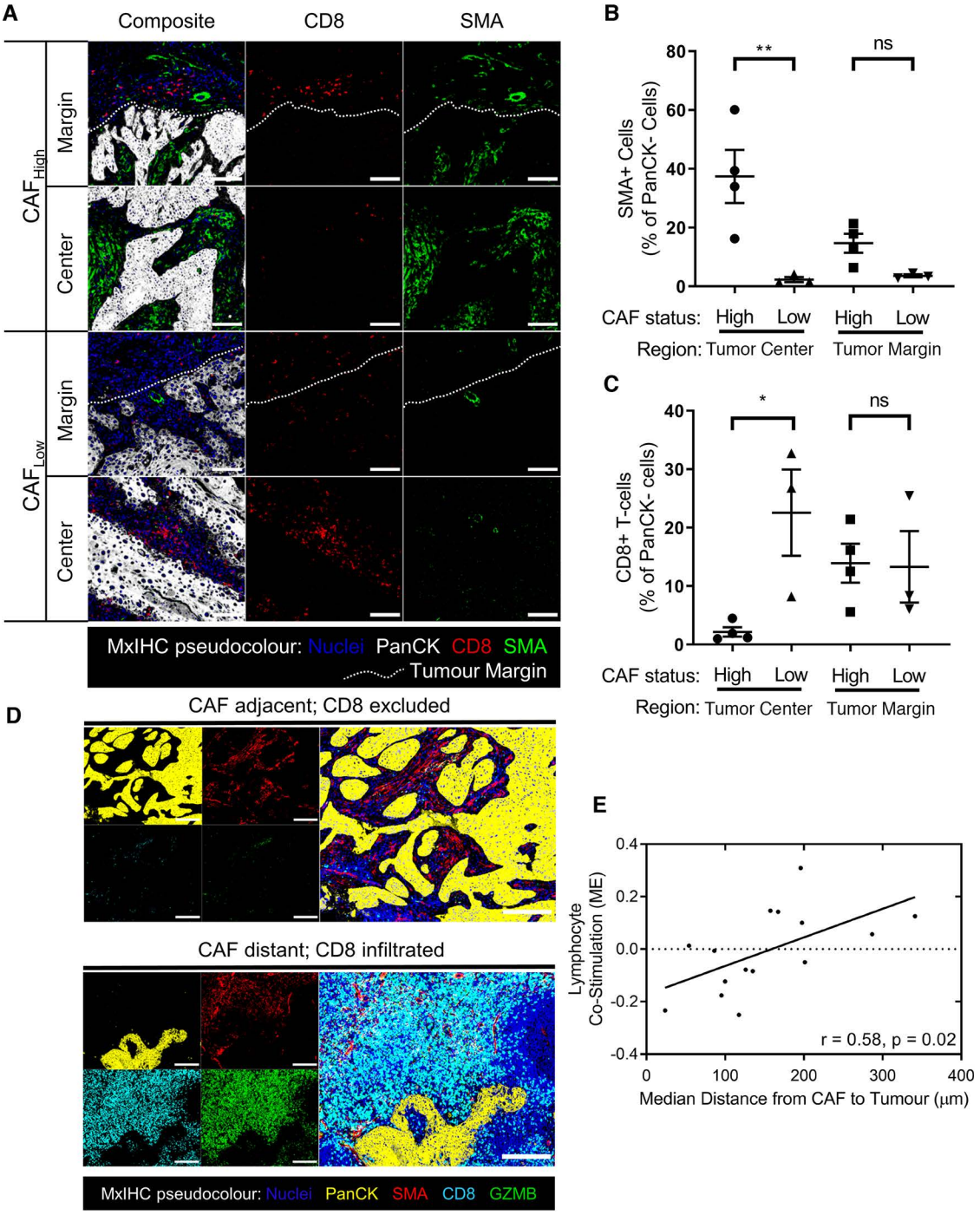
A
Composite
CD8
SMA
CAF High
Margin
Center
CAF Low
Margin
Center
MxIHC pseudocolour: Nuclei PanCK CD8 SMA
Tumour Margin
B
SMA+ Cells (% of PanCK- Cells)
80
60
40
20
0
**
ns
CAF status: High Low High Low
Region: Tumor Center Tumor Margin
C
CD8+ T-cells (% of PanCK- cells)
40
30
20
10
0
*
ns
CAF status: High Low High Low
Region: Tumor Center Tumor Margin
D
CAF adjacent; CD8 excluded
CAF distant; CD8 infiltrated
MxIHC pseudocolour: Nuclei PanCK SMA CD8 GZMB
E
Lymphocyte Co-Stimulation (ME)
0.4
0.2
0.0
-0.2
-0.4
r = 0.58, p = 0.02
0
100
200
300
400
Median Distance from CAF to Tumour (μm)

Figure 4

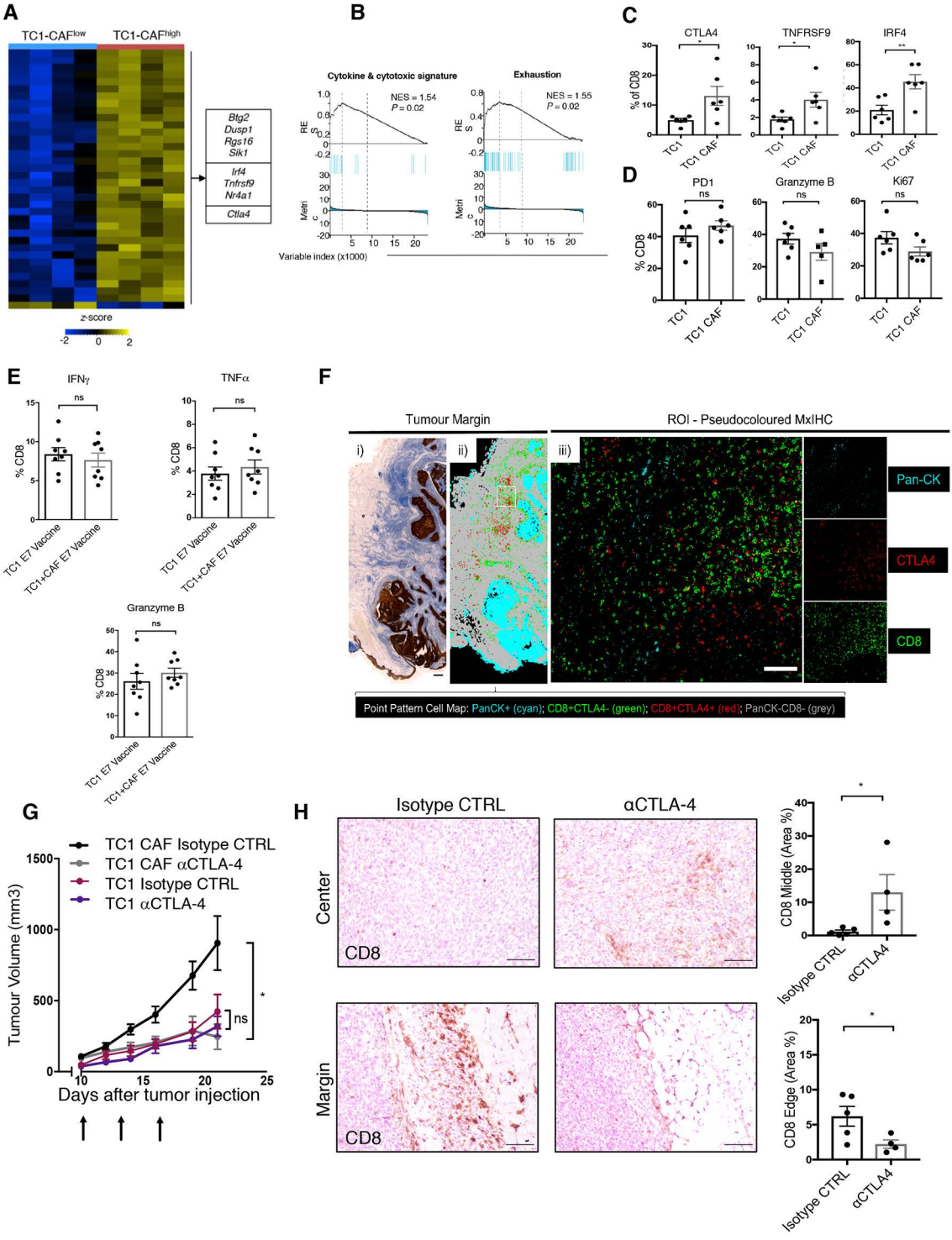
A
TC1-CAFlow
TC1-CAFhigh
z-score
-2
0
2
Btg2
Dusp1
Rgs16
Slk1
Irf4
Tnfrsf9
Nr4a1
Ctla4
B
Cytokine & cytotoxic signature
NES = 1.54
P = 0.02
Exhaustion
NES = 1.55
P = 0.02
RES
Metric
Variable index (x1000)
C
CTLA4
TNFRSF9
IRF4
% of CD8
TC1
TC1 CAF
D
PD1
Granzyme B
Ki67
ns
% CD8
E
IFNγ
TNFα
Granzyme B
TC1 E7 Vaccine
TC1+CAF E7 Vaccine
F
Tumour Margin
ROI - Pseudocoloured MxIHC
i)
ii)
iii)
Pan-CK
CTLA4
CD8
Point Pattern Cell Map: PanCK+ (cyan); CD8+CTLA4- (green); CD8+CTLA4+ (red); PanCK-CD8- (grey)
G
TC1 CAF Isotype CTRL
TC1 CAF αCTLA-4
TC1 Isotype CTRL
TC1 αCTLA-4
Tumour Volume (mm3)
Days after tumor injection
ns
H
Isotype CTRL
αCTLA-4
Center
Margin
CD8
CD8 Middle (Area %)
CD8 Edge (Area %)

Figure 5

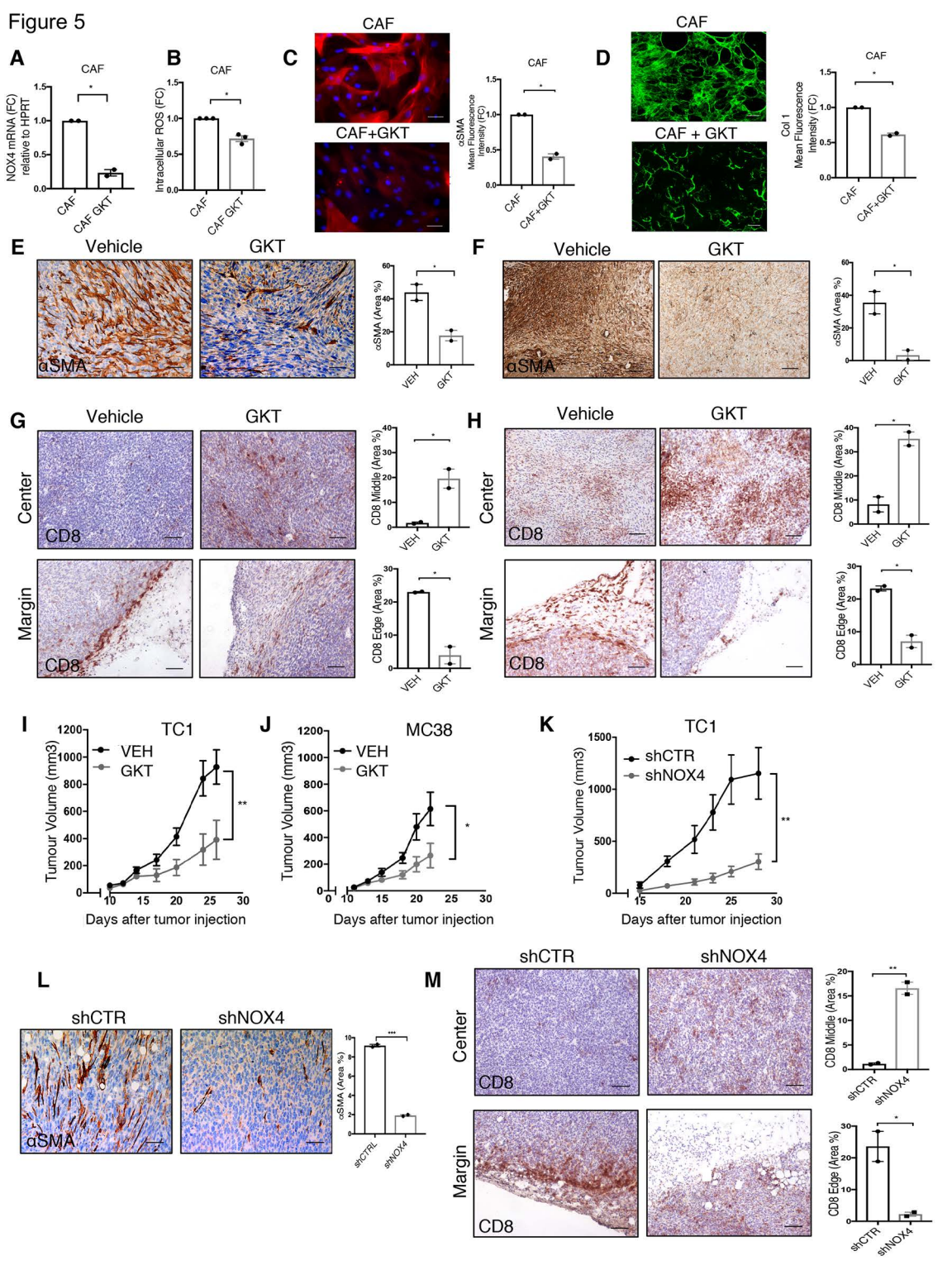
A
CAF
NOX4 mRNA (FC) relative to HPRT
CAF
CAF GKT
B
CAF
Intracellular ROS (FC)
CAF
CAF GKT
C
CAF
CAF+GKT
αSMA Mean Fluorescence Intensity (FC)
CAF
CAF+GKT
D
CAF
CAF + GKT
Col 1 Mean Fluorescence Intensity (FC)
CAF
CAF+GKT
E
Vehicle
GKT
αSMA
αSMA (Area %)
VEH
GKT
F
Vehicle
GKT
αSMA
αSMA (Area %)
VEH
GKT
G
Vehicle
GKT
Center
CD8
CD8 Middle (Area %)
VEH
GKT
Margin
CD8
CD8 Edge (Area %)
VEH
GKT
H
Vehicle
GKT
Center
CD8
CD8 Middle (Area %)
VEH
GKT
Margin
CD8
CD8 Edge (Area %)
VEH
GKT
I
TC1
VEH
GKT
Tumour Volume (mm3)
Days after tumor injection
J
MC38
VEH
GKT
Tumour Volume (mm3)
Days after tumor injection
K
TC1
shCTR
shNOX4
Tumour Volume (mm3)
Days after tumor injection
L
shCTR
shNOX4
αSMA
αSMA (Area %)
shCTRL
shNOX4
M
shCTR
shNOX4
Center
CD8
CD8 Middle (Area %)
shCTR
shNOX4
Margin
CD8
CD8 Edge (Area %)
shCTR
shNOX4

Figure 6

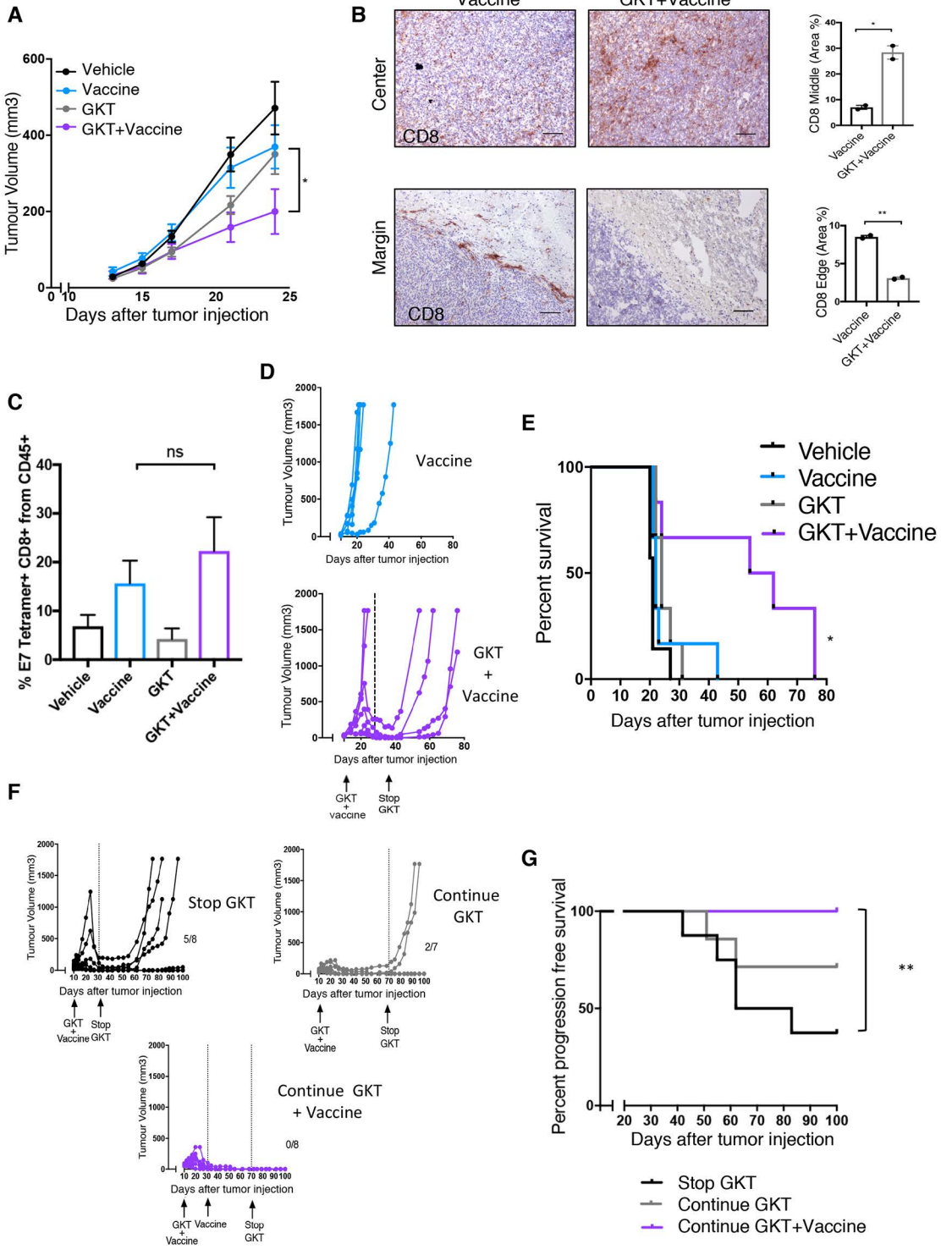
A
Vehicle
Vaccine
GKT
GKT+Vaccine
Tumour Volume (mm3)
Days after tumor injection
B
Vaccine
GKT+Vaccine
Center
Margin
CD8
CD8 Middle (Area %)
CD8 Edge (Area %)
C
% E7 Tetramer+ CD8+ from CD45+
ns
Vehicle
Vaccine
GKT
GKT+Vaccine
D
Tumour Volume (mm3)
Days after tumor injection
GKT + vaccine
Stop GKT
E
Percent survival
F
Stop GKT
5/8
Continue GKT
2/7
Continue GKT + Vaccine
0/8
G
Percent progression free survival
Stop GKT
Continue GKT
Continue GKT+Vaccine

Figure 7

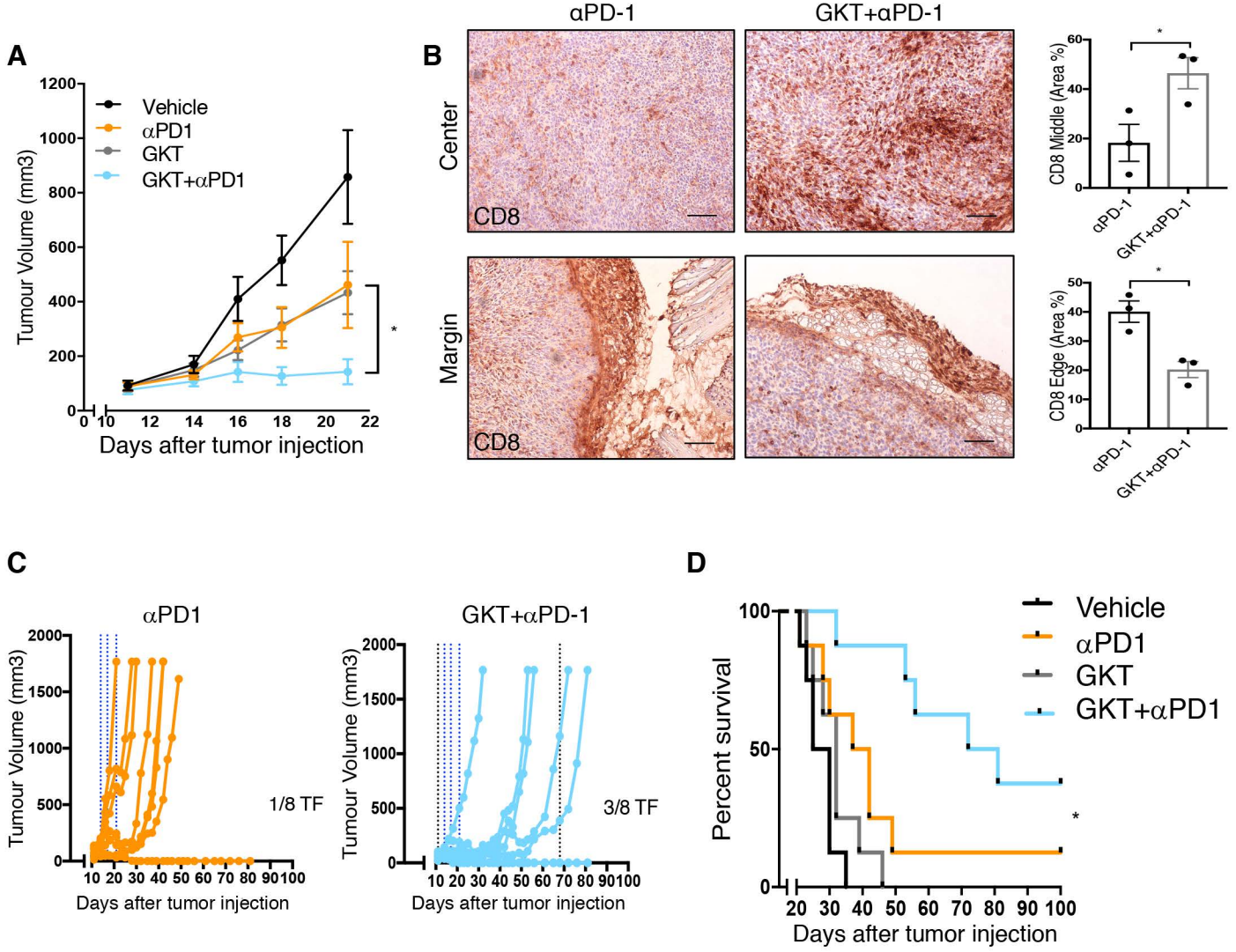
A
Vehicle
αPD1
GKT
GKT+αPD1
Tumour Volume (mm3)
Days after tumor injection
*
B
αPD-1
GKT+αPD-1
Center
Margin
CD8
CD8 Middle (Area %)
CD8 Edge (Area %)
C
αPD1
GKT+αPD-1
Tumour Volume (mm3)
1/8 TF
3/8 TF
Days after tumor injection
D
Vehicle
αPD1
GKT
GKT+αPD1
Percent survival
Days after tumor injection
*